Petroleum Science 23 (2026) 3136–3159

Contents lists available at ScienceDirect

Petroleum Science

journal homepage: www.keaipublishing.com/en/journals/petroleum-science

Original Paper

Grain-size control on lacustrine fan-delta architecture in source-to-sink steep-slope zones: Insights from field surveys and flume-tank experiments

Long Sun [a,b], Sheng-He Wu [a,b,*], Da-Li Yue [a,b,**], Si-Chong Jiang [c], Zhen-Hua Xu [a,b], Ke Zhang [d,e], Li-Jun Yang [a,b], Ji-Ye Li [a,b]

[a] State Key Laboratory of Petroleum Resources and Engineering, China University of Petroleum (Beijing), Beijing, 102249, China
[b] College of Geosciences, China University of Petroleum (Beijing), Beijing, 102249, China
[c] Shenzhen Branch of CNOOC Ltd., Shenzhen, 518054, Guangdong, China
[d] China Zhenhua Oil Co. Ltd, Beijing, 100031, China
[e] Chengdu North Petroleum Exploration and Development Technology Co. Ltd, Chengdu, 610051, Sichuan, China

A R T I C L E I N F O

Article history:
Received 17 August 2025
Received in revised form
28 January 2026
Accepted 21 April 2026
Available online 25 April 2026

Edited by Xiu-Fang Hu

Keywords:
Fan delta
Architectural element
Lobe
Grain size
Source-to-sink steep-slope zones

A B S T R A C T

Lacustrine fan deltas, key depositional systems at basin margins, serve as crucial hydrocarbon accumulation sites. Previous studies have largely focused on depositional slope, overlooking the role of source-area slope and its coupling with grain size in source-to-sink steep-slope zones. Understanding this grain-size control on fan-delta architecture is crucial for predicting subsurface reservoir distribution, dimensions, and stacking patterns. Located in the North China Craton, the Luanping Basin features well-exposed Yuying (Y) and Duiwogoumen (D) sections of the Lower Cretaceous Xiguayuan Formation, which offer ideal outcrops for analyzing fan-delta architecture in source-to-sink steep-slope zones. Unmanned aerial vehicle (UAV) digital models reveal that fan-delta architectural elements in source-to-sink steep-slope zones are dominated by lobes, accompanied by rare distributary channels and slump deposits. Steeper source-area slopes promote high-concentration, high-velocity sediment flows, which favor lobe deposition and suppress erosional channel development, thereby controlling the relative dominance of lobes over channels. Under such steep-slope settings, field surveys and flume-tank experiments jointly elucidate how grain size governs lobe architecture and its underlying mechanisms. Fine-grained sediments exhibit higher fluidity and slower settling rates, enabling broader dispersion and the formation of wide, sheet-like lobes with high width-to-thickness ratios and predominantly vertical stacking. In contrast, coarse-grained sediments show lower fluidity, poorer stability, and faster settling, leading to rapid deposition that produces narrow, tongue-shaped lobes with low width-to-thickness ratios, dominated by lateral migration and associated with deeper incised channels. Thus, fan-delta architecture in source-to-sink steep-slope zones is governed by a dual control: source-area slope determines the lobe-dominated pattern, and grain size dictates lobe geometry and stacking. This study provides a mechanistic framework for predicting reservoir distribution in analogous systems.

1. Introduction

Fan deltas are basin-margin depositional systems that develop where alluvial fans prograde directly from adjacent highlands into bodies of standing water (Holmes, 1945; McPherson et al., 1987). In continental basins, lacustrine fan-delta reservoirs represent significant hydrocarbon plays. Their substantial internal heterogeneity has sustained extensive research interest in petroleum geology and sedimentology (Li et al., 2021; Liu et al., 2019; Sun et al., 2024; Tan et al., 2017; Tanaka and Maejima, 1995; Wu

* Corresponding author.
** Corresponding author.
E-mail addresses: reser@cup.edu.cn (S.-H. Wu), yuedali@cup.edu.cn (D.-L. Yue).
Peer review under the responsibility of China University of Petroleum (Beijing).

https://doi.org/10.1016/j.petsci.2026.04.036

et al., 2025). Characterized by dual subaerial–subaqueous deposition and complex source-to-sink configurations, they form critical links within sediment routing systems and exhibit intricate depositional architecture (Kataoka and Nakajo, 2004; Postma, 1990; Sun et al., 2025).

The formation of fan deltas is governed by the coupled controls of source and depositional conditions. Source conditions include grain size, flow velocity, sediment concentration, and source-area slope, whereas depositional conditions encompass depositional slope and water depth (Zhang et al., 2021). Slope is a pivotal parameter in the source-to-sink system, directly or indirectly influencing weathering, transport, and deposition in both the catchment and the basin (Hussain et al., 2020; Sun et al., 2025). Previous studies have largely focused on the slope of the depositional area, classifying fan deltas into steep-slope and gentle-slope types based on this gradient (Wu et al., 1994; Yu et al., 2014). Research has detailed how depositional slope provides a key driving force for sediment transport and controls fan-delta morphology by regulating flow velocity (Gao et al., 2020; Harvey et al., 2005; Parker et al., 1998). Numerous experimental simulations have further explored the relationships among fan slope, sedimentation patterns, and flow dynamics by varying depositional conditions (Geleynse et al., 2011; Milana and Tietze, 2002; Nota et al., 2024; Whipple et al., 1998; Zhang et al., 2021, 2022). These studies underscore the fundamental role of depositional slope in sedimentary system evolution and its importance for understanding sedimentary dynamics (Sun et al., 2025). However, as proximal deposits, fan deltas are profoundly influenced by their source area. A key oversight from a source-to-sink perspective is the role of the source-area slope. While depositional slope primarily affects morphology through flow velocity (Gao et al., 2020), the source-area slope exerts a more comprehensive control by also governing sediment concentration, discharge, and the initial grain-size distribution (Sun et al., 2025). Under specific climatic conditions, steep mountainous catchments are more susceptible to slope failures, such as landslides and collapses, which increase debris supply and promote high-concentration, high-velocity debris flows (de Haas et al., 2016; Shanmugam, 2000). Despite this, how the source-area slope controls the internal architecture of fan deltas remains poorly understood. Furthermore, although physical experiments have simulated steep-slope fan deltas by adjusting the depositional gradient, they often retain source-condition parameters (e.g., low concentration and discharge) typical of gentle-slope catchments (Zhang et al., 2021, 2022). Conversely, subsurface and field studies have focused on reconstructing paleotopography of the depositional areas or have been limited by data, making it difficult to quantify the source-area slope and its effects on sediment flux (Li et al., 2021; Sun et al., 2025; Zhang et al., 2023). Therefore, the steep-slope zone emphasized in this study extends beyond the steep depositional or fault-related slopes commonly examined. It refers specifically to a source-to-sink steep slope zone where both the source and the depositional basin exhibit steep gradients. Within this framework, studying fan-delta architecture as an integrated system remains an underexplored research gap, particularly for fan deltas widely developed in such steep slope settings.

Extensive physical experiments and numerical simulations have elucidated how sediment grain size controls fan-delta processes, morphology, and vertical rhythms (Van Dijk et al., 2009, 2012; Wang et al., 2015; Zhang et al., 2021, 2022). Key findings include: (1) grain size influences the morphology and scale of architectural elements, with coarser sediment leading to slower progradation, flatter fan profiles, smaller width-to-thickness ratios, and larger distributary channels; (2) the critical slope for fan-delta development is negatively correlated with median grain size, with finer grains promoting sheet flows and lobe development; and (3) grain size affects lobe accretionary rhythms, as demonstrated by coarser sediments producing fining-upward sequences. However, even studies that varied grain size and depositional slope in experiments have largely maintained source-condition parameters typical of gentle topography, neglecting the steep source-area slope's control on sediment supply and flow behavior (Wang et al., 2015; Zhang et al., 2021, 2022). Consequently, the sedimentary dynamics and the controlling role of grain size on fan-delta architecture within integrated source-to-sink steep-slope zones are still insufficiently understood.

We hypothesize that in steep source-to-sink systems, grain size exerts a primary control on lobe geometry and stacking pattern, while channels remain subordinate. To test this, we integrate field surveys with flume-tank experiments through a three-part methodology: (1) lithofacies analysis based on field measurements, (2) cross-sectional architecture analysis using 3D digital outcrop models constructed from unmanned aerial vehicle (UAV) data, and (3) interpretation of sedimentary dynamics governing fan delta formation in source-to-sink steep-slope zones, combined with flume-tank experiments using grain size as the sole variable. Ultimately, this will establish architectural patterns for fan deltas under varying grain size conditions in source-to-sink steep-slope zones.

2. Geological setting

The outcrop sections investigated in this study are located in the Luanping Basin, situated in the northeastern part of the Yanshan Fold-Thrust Belt on the North China Craton (Fig. 1(a)) (Cope and Graham, 2007; Fang et al., 2022; Wei et al., 2012). This basin is a continental volcanic-faulted lake basin with a NE–SW-trending half graben structure. The basin extends approximately 40 km in the NE–SW orientation and approximately 20 km in the NW–SE direction, with a remaining area of approximately 800 km^2 (Pan et al., 2021; Yan et al., 2020; Zhang et al., 2023). Its tectonic framework is primarily controlled by two extensional normal faults: the Hongqi-Gangzi Fault to the north and the Xiaobaiqi-Fujiadian Fault to the west (Fig. 1(b)) (Cope et al., 2010). The tectonic evolution of the basin is divided into three stages: (1) the first rifting stage (initial rifting), (2) the second rifting stage (peak rifting), and (3) the third rifting stage (rifting decline), during which two phases of large-scale volcanic activity occurred (Fig. 2(a)) (Jia et al., 2020; Wu et al., 2000).

Basement rocks of the Luanping Basin consist predominantly of Neoarchean metamorphic rocks and Proterozoic intrusive rocks (Pan et al., 2021; Yan et al., 2020). In ascending order, the stratigraphy comprises the Middle Jurassic Jiulongshan Formation (J_2j), Upper Jurassic Tiaojishan Formation (J_3t), Upper Jurassic Houcheng Formation (J_3h), Lower Cretaceous Zhangjiakou Formation (K_1z), Lower Cretaceous Dabeigou Formation (K_1db), Lower Cretaceous Dadianzi Formation (K_1d), Lower Cretaceous Xiguayuan Formation (K_1x), and Quaternary (Q) (Fig. 2(a)). This study focuses on the Lower Cretaceous Xiguayuan Formation (K_1x). The biotite $^{40}Ar/^{39}Ar$ age of the extensively developed basalts within the Lower Cretaceous Xiguayuan Formation of the Luanping Basin constrains the depositional age to ~128.4 $\pm$ 0.2 Ma, and the total thickness of the K_1x is approximately 1700 m (Wei et al., 2012; Yuan et al., 2025). The formation consists mainly of conglomerate, sandstone, siltstone, and mudstone, interpreted as deposits of alluvial fans, fan deltas, and semi-deep to deep lakes. From bottom to top, it comprises a complete second-order sequence (characterized by an initial lacustrine transgression followed by a lacustrine regression), which can be further subdivided into three third-order sequences (Fig. 2(b)). The lacustrine

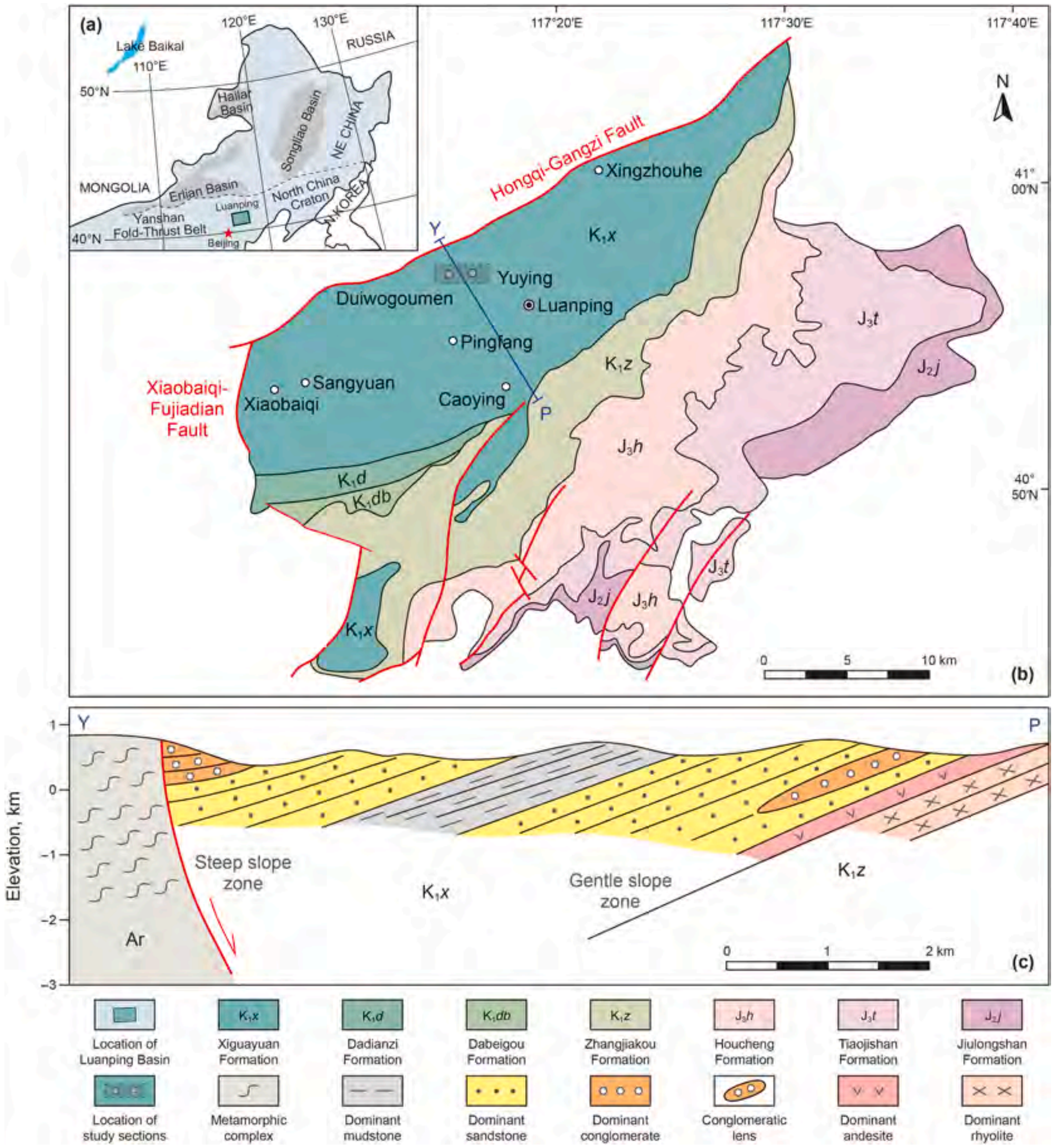

Fig. 1. **(a)** Regional location map of the Luanping Basin within the North China Craton; **(b)** geological map showing the distribution of strata and faults in the Luanping Basin (modified from Ma et al., 2023; Sun et al., 2026; Yan et al., 2020); **(c)** geological cross section displaying the internal architecture of the Luanping Basin, with the section location shown in (b) (modified from Wei et al., 2012).

mudstone of the Xiguayuan Formation has good hydrocarbon generation potential, while the fan delta and alluvial fan sand bodies serve as reservoirs. These intervals have been the preferred targets for oil and gas exploration in recent years, and hydrocarbon shows have been discovered (Pan et al., 2021).

During the deposition of the Xiguayuan Formation, the northern part of the basin was controlled by a large synsedimentary normal fault and proximity to the source area, representing a steep-slope zone of the lacustrine basin; in contrast, the southern part, distal to the source area, formed a gentle-slope zone (Fig. 1(c)) (Cope et al., 2010; Wei et al., 2012). The two outcrop sections in this study, the Yuying (Y) section and the Duiwogoumen (D) section, are both located near this fault in the northern basin (Fig. 1(b)) and represent typical lacustrine fan-delta front deposits within the source-to-sink steep-slope zones. Sedimentary structures such as gravel bedding plane dips indicate that the source direction of both sections is northwest, with a paleocurrent direction of 145° (Fig. 3(a)) (Wei et al., 2012).

The Y section has a total length of approximately 270 m, with a cumulative thickness of the clastic succession of 29.6 m. Based on strike, it is subdivided into two segments oriented at 126° and 112° (Fig. 3(a) and (b)). The angle between the paleocurrent direction and the section strike ranges from 19° to 33°, indicating a low-angle oblique relationship to the source. Stratigraphically, it belongs to the upper sequence of the Xiguayuan Formation and exhibits an overall coarsening-upward succession. Dominant lithologies include poorly sorted sandstone, pebble conglomerate, cobble conglomerate, glutenite, and mudstone (Fig. 2(c)). The D section is approximately 305 m long with a cumulative clastic thickness of 21.4 m. It is similarly subdivided into two segments with strikes of 104° and 89° (Fig. 3(a)–(c)). The angle between section strike and paleocurrent direction (41°–56°) reflects a high-angle oblique source direction. Main lithologies comprise cobble conglomerate, pebble conglomerate, glutenite, minor sandstone, and gray-green mudstone (Fig. 2(c)) (Yang et al., 2021).

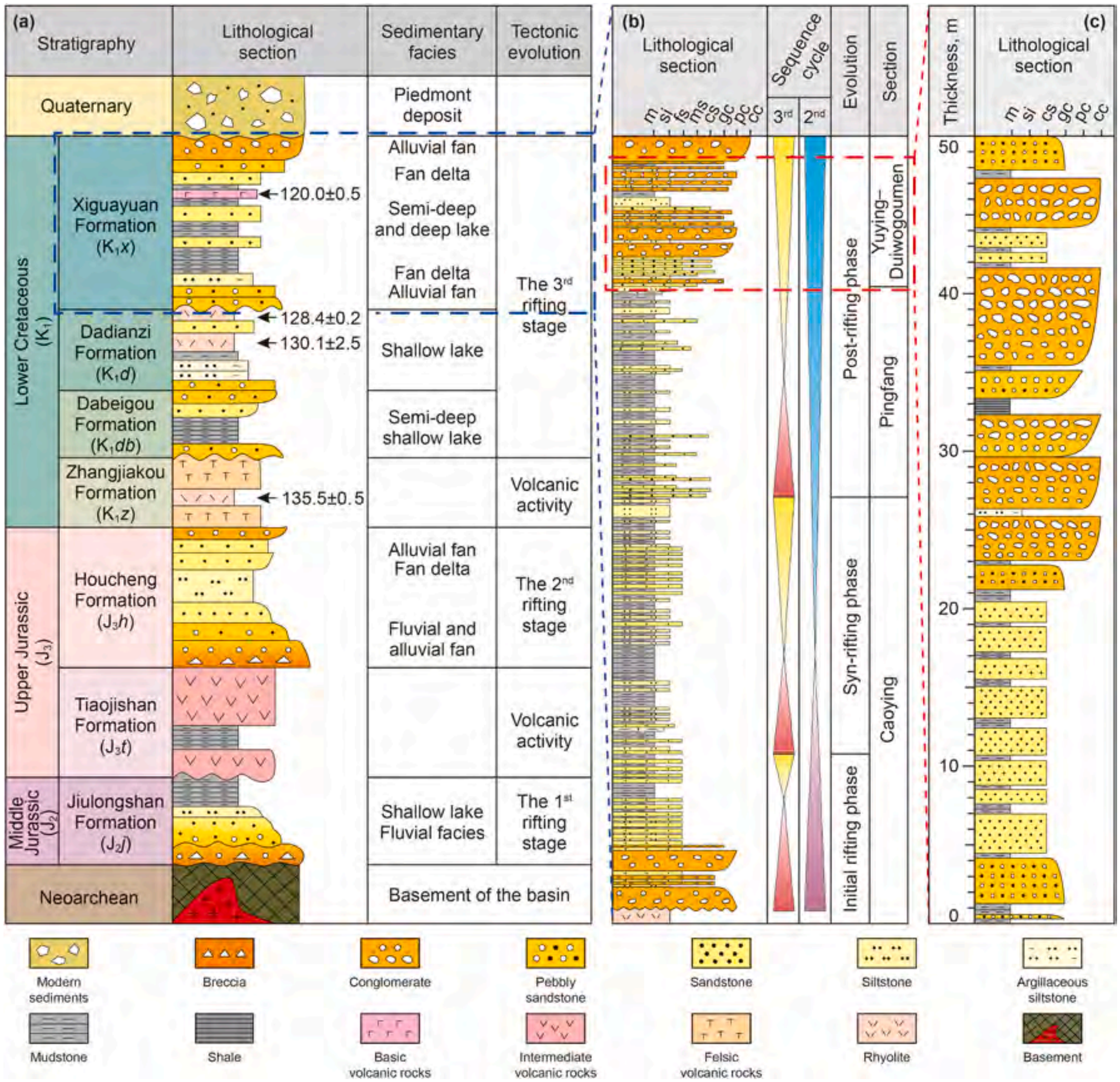

Fig. 2. Stratigraphic column and lithological section of study interval. **(a)** Generalized stratigraphic and lithological column showing geochronology, sedimentary facies and tectonic evolution for all successions in the Luanping Basin (modified from Pan et al., 2021); **(b)** lithological section and sequence cycles for the Xiguayuan Formation in central parts of the basin, with section location shown in Fig. 1(b); **(c)** lithology and thickness of the two study sections (modified from Sun et al., 2026). Note: m, si, fs, ms, cs, gc, pc, and cc represent mudstone, siltstone, fine sandstone, medium sandstone, coarse sandstone, granule conglomerate, pebble conglomerate and cobble conglomerate, respectively.

3. Methodology

3.1. Field survey methodology

3.1.1. Field measurement

This study combined traditional field measurement with UAV-based digital observation. Field measurements focused on two outcrop sections and included detailed observations of (1) sedimentary petrological characteristics: lithology, grain size, sorting, roundness, and sedimentary structures; (2) depositional architectural element characteristics: morphological features, directions, dimensions, and stacking patterns. A total of 435 high-resolution photographs were captured using a Nikon D800E camera, and measured sections with a cumulative thickness exceeding 50 m were documented. Additionally, 23 samples were collected for thin section analysis, and 43 samples were collected for grain-size analysis via combined sieve analysis and laser diffraction. All analyses were performed at the State Key Laboratory of Petroleum Resources and Engineering, China University of Petroleum (Beijing).

3.1.2. Unmanned aerial vehicle observation

UAV-based digital observation is a research method involving the collection of coordinate data from multiple directions and angles to construct a 3D digital outcrop model of the study area (Zhang et al., 2023). The primary advantage of UAV-based observation is its ability to acquire data from steep outcrops and other inaccessible areas beyond the reach of traditional field surveys (Yin et al., 2023). Furthermore, the 3D digital outcrop model generated from UAV data facilitates quantitative analysis of architectural elements, effectively minimizing measurement errors and significantly enhancing the accuracy of field research (Blistan et al., 2016; Zhang et al., 2023). For this field campaign, a DJI M600PRO UAV equipped with a high-definition camera featuring five oblique lenses and a maximum flight altitude of 300 m was employed. Using a systematic grid flight pattern (Fig. 3(b) and (c)), a total of 2119 high-definition, geotagged photos (containing longitude, latitude, and elevation data) were captured. Context Capture v.2.0 software was then used to construct the 3D digital outcrop models of the two study sections, achieving a resolution of 0.1 m.

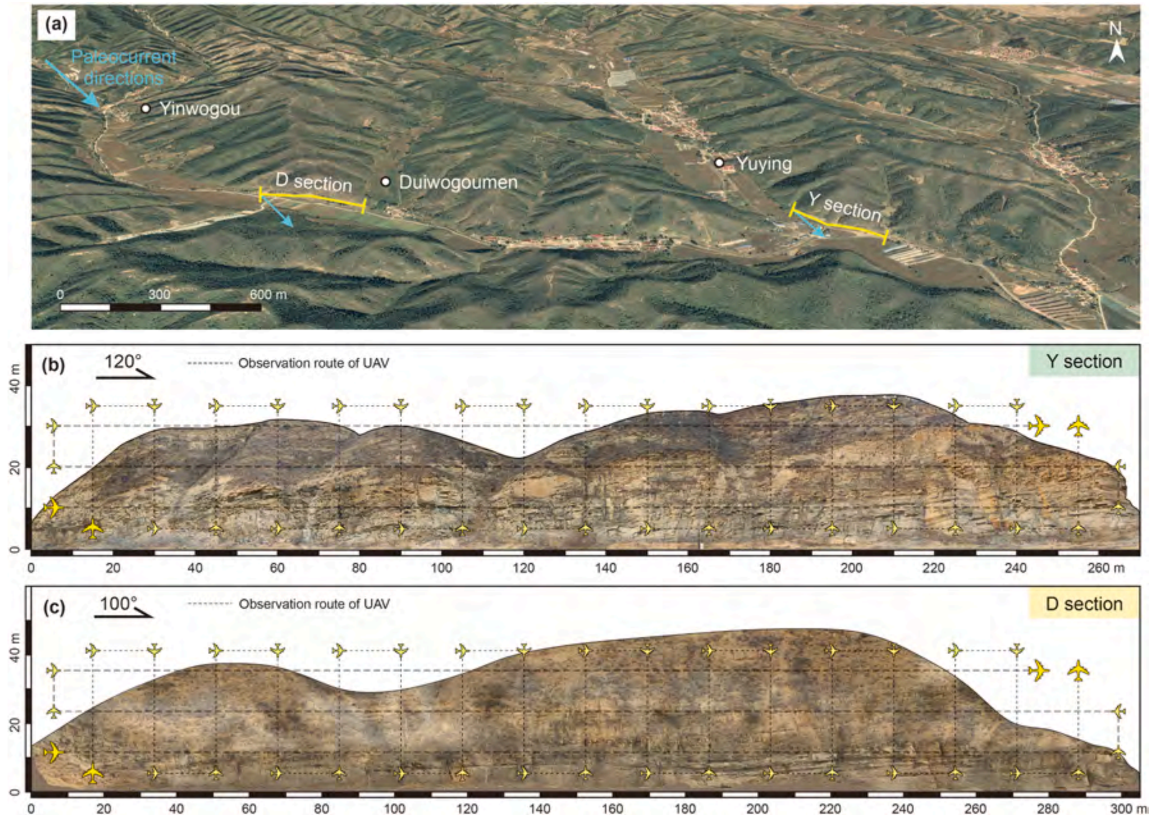

Fig. 3. (a) Satellite imagery showing locations and orientations of the study sections. **(b)–(c)** 3D digital models established using UAV data for the study sections Yuying (Y) and Duiwogoumen (D), respectively.

3.2. Flume-tank experiment methodology

3.2.1. Design of flume-tank experiments

Three fan delta flume-tank experiments (R1–R3) were conducted using a sedimentation simulation experimental device at the Sedimentology–Stratigraphy Dynamics Experimental Platform of the State Key Laboratory of Petroleum Resources and Engineering, China University of Petroleum (Beijing). The experimental system consists of: (a) a slurry sediment supply system, (b) a 4 m × 9 m pool equipped with a two-stage slope adjustment device, (c) a high-definition imaging system, and (d) a 3D laser scanner (Fig. 4). The slurry sediment supply system delivers high-concentration sediments, with freely adjustable sediment grain size, concentration, flow velocity and discharge according to experimental requirements. The slope adjustment device has a variable gradient range of 0–90‰, corresponding to slope angles of 0–5.1°, encompassing the gradient ranges of most natural sedimentary environments. The high-definition imaging system documents the formation and evolution processes of sedimentation, while the 3D laser scanner performs geomorphic reconstruction and thickness measurement.

This study aims to clarify the depositional architecture of fan deltas in source-to-sink steep-slope zones under varying sediment grain sizes and to elucidate the underlying control mechanisms. Experimental parameters were scaled-down sedimentary dynamics parameters derived from the outcrops. In addition to reconstructing key field parameters (e.g., flow rate, sediment concentration, and slope) using sedimentary dynamics formulas, the experimental design was validated by comparing thresholds with modern sediments. The Wuma fan delta in Lugu Lake, southwestern China, was selected as a representative analog for steep slopes. Key experimental parameters included hydrodynamic indices such as mean flow velocity (U), Froude number (Fr), Reynolds number (Re), bed slope (S), volumetric sediment concentration (C_v), and median grain size (D_{50}).

Key parameters were determined as follows:

The paleo-slope of the depositional area was estimated using the following empirical relationship:

$$S = 0.141\frac{D_{max}}{H} \tag{1}$$

where S is the paleo-slope gradient, m/m; D_{max} is the maximum gravel size, m; H is the flow layer depth, m.

For sediment grains >0.2 mm, the average flow velocity was estimated from the critical velocity (Sidorchuk and Borisova, 2000):

$$U_c = 6.8D_{50}^{1/3}H^{1/6} \tag{2}$$

$$U = 0.76U_c\left(\frac{H}{D_{10}}\right)^{1/6} \tag{3}$$

where, U_c is the critical velocity, m/s; D_{50} is the median sediment grain size, m; U is the average velocity, m/s; D_{10} is the coarse fraction grain size (corresponding to 10% cumulative percentage), m.

The flow regime was characterized by the Froude number (Fr) and Reynolds number (Re) (Van Dijk et al., 2009):

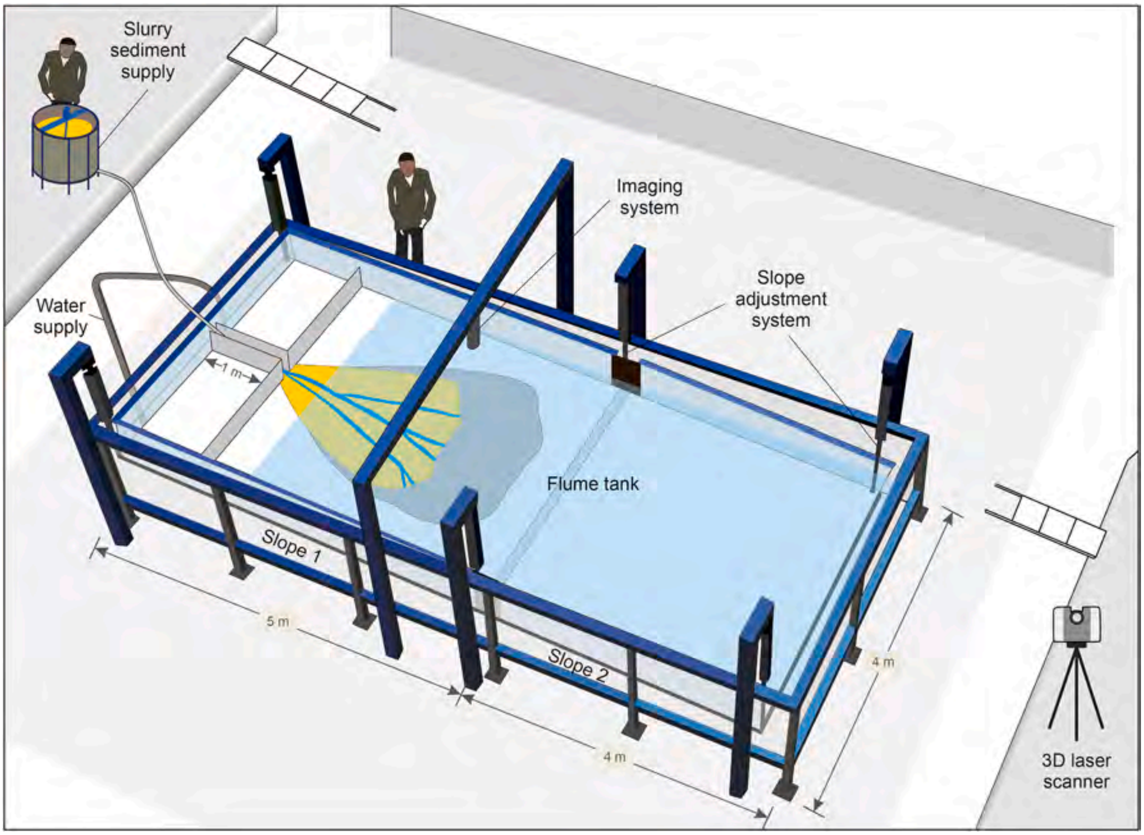

Fig. 4. Schematic view of the flume-tank experimental setup, showing the slurry sediment supply device, slope adjustment system, imaging system, and 3D laser scanner.

$$\mathrm{Fr} = \frac{U}{\sqrt{gH}} \tag{4}$$

$$\mathrm{Re} = UH/\mu \tag{5}$$

where g is the gravitational acceleration, m/s^2; μ is the kinematic viscosity of water, m^2/s. Here, Fr distinguishes between subcritical (Fr < 1) and supercritical (Fr > 1) flow, while Re differentiates between laminar (Re < 40) and turbulent (Re > 2000) regimes.

To ensure dynamic similarity between the experiments and the natural system, scaling was performed based on similarity theory. Due to scale effects, grain-size parameters for the experiments were obtained by scaling the field-derived grain-size distributions, guided by dimensionless numbers that characterize sediment transport (de Leeuw et al., 2016; Parker et al., 2003; Shields, 1936; van Rijn, 1984). Among them, the Shields number (τ^*) is used to characterize the sediment transport intensity and mobility (Shields, 1936), the critical Shields number (τ^*_c) is used to calculate the critical starting condition when the sediment starts to move, and the ratio (T) of the τ^* to τ^*_c can be used to reflect the transport intensity of sediments (Parker et al., 2003). The larger the T value, the greater the transport intensity of the sediments. Particle Reynolds number ($\mathrm{Re_p}$) is used to reflect the stability of sediment in the fluid (Parker et al., 1998). The explicit equations are as follows:

$$T = \tau^* / \tau^*_c \tag{6}$$

$$\tau^* = \frac{\tau_b}{\rho R g D_{50}} \tag{7}$$

$$\tau_b = \rho g H S \tag{8}$$

$$R = \frac{\rho_s - \rho}{\rho} \tag{9}$$

$$\tau^*_c = 0.5\left[0.22\mathrm{Re_p}^{-0.6} + 0.06 \times 10^{\left(-7.7\mathrm{Re_p}^{-0.6}\right)}\right] \tag{10}$$

$$\mathrm{Re_p} = \frac{D_{50}\sqrt{RgD_{50}}}{\mu} \tag{11}$$

where τ_b represents the average shear stress, N/m^2; ρ is fluid density, kg/m^3; R is the submerged specific gravity of sediment, dimensionless; ρ_s is the density of the sediment, kg/m^3; μ denotes the kinematic viscosity of water, approximately 10^{-6} m^2/s at 20 °C.

Specific calculated parameter values, which depend on final grain size, flow depth, and unit thickness, are provided in the Results section following the petrological and architectural analysis.

3.2.2. *Measurement of experimental results*

Depositional evolution was monitored using a high-definition imaging system and a 3D laser scanner. Positioned directly above the flume tank, the imaging system comprised four high-definition cameras programmed to capture images at 1-s intervals during simulations. Concurrently, a Leica RTC360 3D laser scanner acquired point cloud data of depositional bedforms and fan-delta surfaces at 1 mm vertical and horizontal resolution. Post-processing with Leica Cyclone 2023 software generated high-resolution 3D digital terrain models and sediment thickness contour maps. Post-experiment, fan-delta sediments were oven-dried at 30 °C for 48 h. Six section lines were established along two orientations, namely parallel to the sediment source and perpendicular to the sediment source. Sequential sectioning, observation, description, and photography of these sections yielded detailed sedimentary cross-section datasets.

4. Results

4.1. Lithology of outcrop section

Based on distinct grain-size sequences, five major lithologies are defined and described, including conglomerate, glutenite, sandstone, siltstone and mudstone. Combining with sedimentary structures, sixteen lithofacies subtypes are subdivided (Figs. 5 and 6).

4.1.1. Conglomerate lithofacies

In this type of lithofacies, clasts larger than 2 mm account for more than 50% of the composition. The main subtypes include massive cobble conglomerate (Ccm), massive pebble conglomerate (Cpm), graded pebble conglomerate (Cpg), massive granule conglomerate (Cgm), graded granule conglomerate (Cgg), cross-stratified granule conglomerate (Cgc), and parallel-stratified granule conglomerate (Cgp) (Fig. 5(a)–(g)).

(1) Ccm

Description: The Ccm lithofacies is a massive, clast-supported conglomerate in which cobbles (>100 mm) constitute over 50% of the framework. Dominant clast sizes range from 120 mm to 200 mm (maximum 430 mm), with minor pebbles. The interstices are filled with finer debris. Clasts are moderately rounded (sub-angular to sub-rounded). The fabric is chaotic, sorting is extremely poor, and near-upright clasts are present (Fig. 5(a)).

Interpretation: This lithofacies is interpreted as debris-flow deposits. The extremely poor sorting, chaotic fabric, and near-upright clasts indicate rapid “freezing” of a cohesive flow, which prevented clast reorientation (Kim et al., 1995; Sohn et al., 1999).

(2) Cpm

Description: The Cpm lithofacies is a massive, pebble-dominated conglomerate, in which pebbles (10–100 mm) constitute over 50% of the framework. Pebble content reaches ~80%, with dominant grain sizes of 15–30 mm. Outsized cobbles (up to 400 mm) occur as floating clasts within the pebble-rich, sandy matrix. Clasts are moderately rounded (sub-angular to sub-rounded), exhibiting a disordered fabric and poor to extremely poor sorting (Fig. 5(b)).

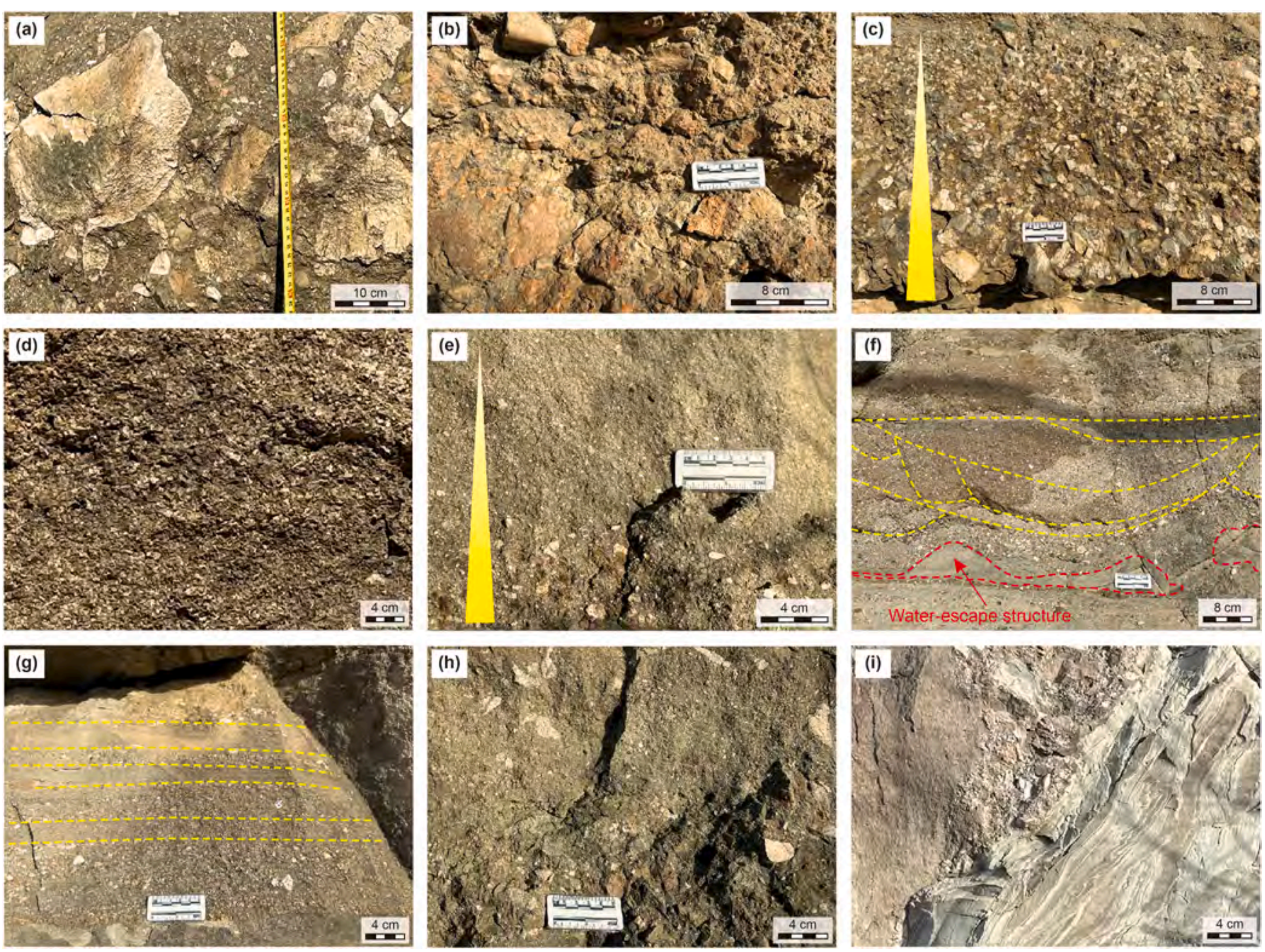

Fig. 5. Photographs showing representative conglomerate and glutenite lithofacies of the two study sections. **(a)** Massive cobble conglomerate (Ccm); **(b)** massive pebble conglomerate (Cpm); **(c)** graded pebble conglomerate (Cpg); **(d)** massive granule conglomerate (Cgm); **(e)** graded granule conglomerate (Cgg); **(f)** cross-stratified granule conglomerate (Cgc); **(g)** parallel-stratified granule conglomerate (Cgp); **(h)** massive glutenite (Gm); **(i)** slump-generated glutenite (Gs).

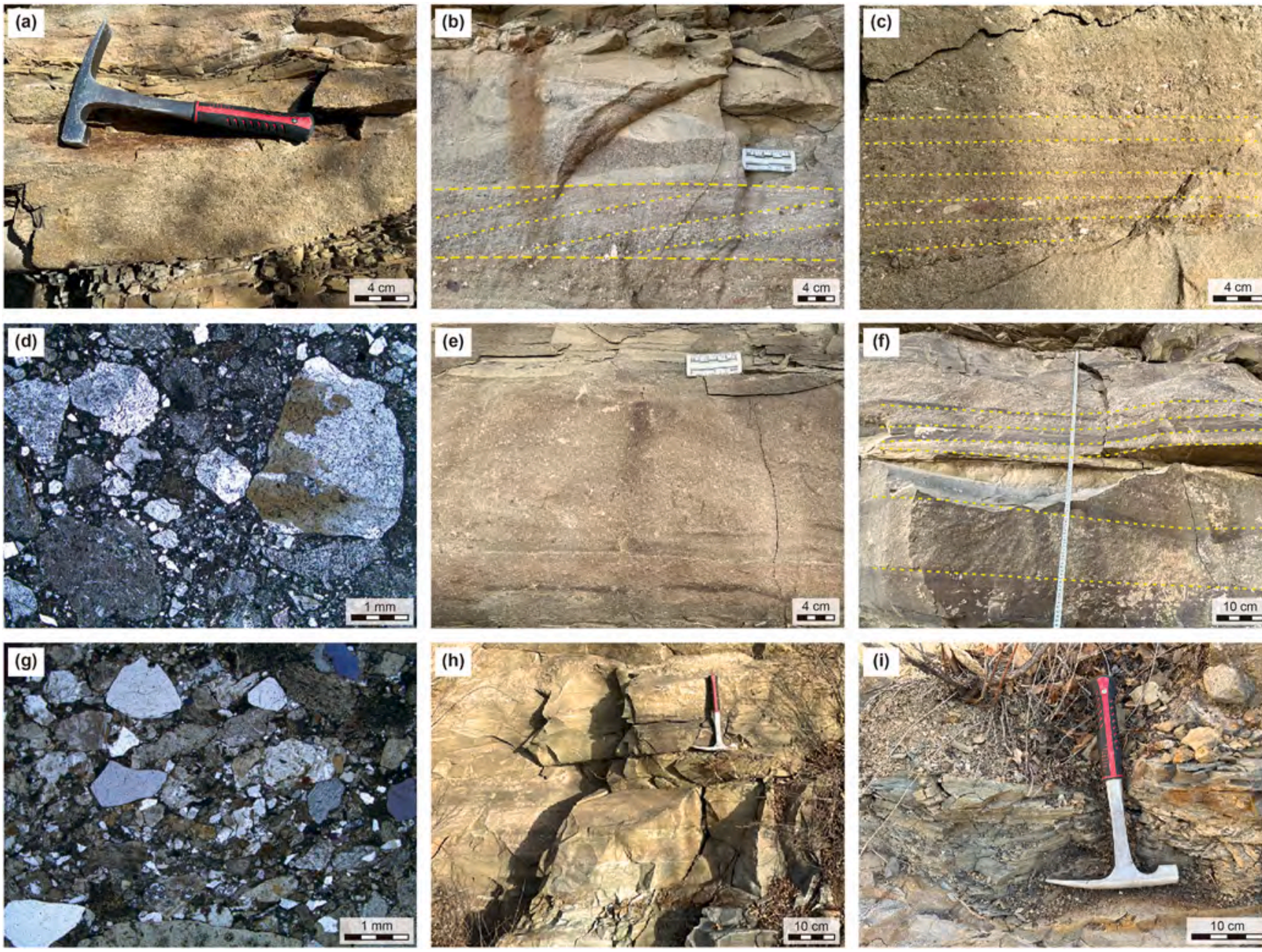

Fig. 6. Photographs and microscopy images exhibiting representative sandstone and mudstone lithofacies of the two study sections. **(a)** Massive heterogranular sandstone (Shm); **(b)** cross-stratified heterogranular sandstone (Shc); **(c)** parallel-stratified heterogranular sandstone (Shp); **(d)** microscopy images of heterogranular sandstone; **(e)** massive fine–medium sandstone (Sfm); **(f)** parallel-stratified fine–medium sandstone (Sfp); **(g)** microscopy images of fine–medium sandstone; **(h)** horizontal-laminated siltstone (Sih); **(i)** horizontal-laminated mudstone (Mh).

Interpretation: This lithofacies is interpreted as debris-flow deposits. Compared to more cobble-dominated debris flows (e.g., Ccm), it likely represents events with a higher sand-to-gravel ratio or slightly longer transport distance.

(3) Cpg

Description: The Cpg lithofacies is a pebble conglomerate with well-developed normal grading. Pebbles constitute ~60% of the rock, and the average clast diameter fines upward from 50 mm at the base to 5 mm at the top. Clasts exhibit point contacts, are moderately rounded (sub-angular to sub-rounded), and are well sorted (Fig. 5(c)).

Interpretation: This lithofacies is interpreted as a pebbly high-density turbidite. The distinct normal grading records deposition from a single waning, turbulent current (Zavala and Pan, 2018).

(4) Cgm

Description: The Cgm lithofacies is a massive, matrix-supported conglomerate dominated by granules (2–10 mm), which comprise >50% (locally >90%) of the composition. The framework is infilled by a sandy-gravelly matrix. Clasts are moderately rounded (sub-rounded to sub-angular) and exhibit moderate sorting (Fig. 5(d)).

Interpretation: This lithofacies is interpreted as sandy debris-flow deposits. The matrix-supported, massive structure indicates rapid deposition from a cohesive flow.

(5) Cgg

Description: The Cgg lithofacies consists of graded-bedded conglomerate where granules (2–10 mm) constitute >50% of the composition. Clast diameter fines upward from 10 mm to 2 mm, with coarse sand (1–2 mm) dominating the uppermost part. Clasts are moderately rounded (sub-angular to sub-rounded) and moderately sorted (Fig. 5(e)).

Interpretation: This lithofacies is interpreted as granule-dominated high-density turbidites. The normal grading records deposition from a single, waning turbulent flow (Lowe, 1982; Zavala and Pan, 2018).

(6) Cgc

Description: The Cgc lithofacies is a cross-stratified conglomerate in which granules (2–10 mm) constitute >50% of the framework (locally ~60%). It exhibits medium-scale trough cross-stratification, featuring a distinct basal scour surface where gravel-rich flows eroded underlying sandstone. This contact is marked by an abrupt grain-size transition and water-escape structures. Minor basal pebbles (up to 20 mm) are present. Clasts are well-rounded (predominantly sub-rounded), show a preferred orientation parallel to bedding, and are moderately sorted (Fig. 5(f)).

Interpretation: This lithofacies records sustained tractive flow. The trough cross-stratification, basal scour, and oriented clasts distinguish it from debris-flow and turbidity-current deposits in the system (Yan et al., 2020).

(7) Cgp

Description: The Cgp refers to parallel-stratified conglomerates with granule (2–10 mm) content exceeding 50%. Granules constitute ~70% of clasts, with a mean diameter of 4 mm. A fining-upward sequence is present: basal gravels average 6 mm and fine upward. Locally, floating pebbles (up to 15 mm) occur, some showing near-vertical imbrication. Clasts are moderately rounded (sub-rounded to sub-angular), exhibit a strong preferred orientation parallel to bedding, and are moderately sorted (Fig. 5(g)).

Interpretation: This lithofacies is interpreted as deposits of waning, upper-flow-regime tractive currents, possibly associated with flood events. Parallel stratification and grading indicate tractive transport and flow deceleration, while local floating clasts suggest episodic rapid dumping (Zavala and Pan, 2018).

4.1.2. Glutenite lithofacies

Based on sedimentary structural characteristics, the glutenite lithofacies is subdivided into massive glutenite (Gm) and slump-generated glutenite (Gs) (Fig. 5(h) and (i)).

(1) Gm

Description: The Gm lithofacies is a diamictite with massive structure, where neither gravel nor sand exceeds 50% individually, but their combined content exceeds 50%. In the study sections, it contains ~45% gravel and ~40% sand, is predominantly clast-supported, and has local matrix-supported zones where the mud content is <15%. Clasts are moderately rounded (sub-rounded to sub-angular), chaotically arranged, and poorly sorted (Fig. 5(h)).

Interpretation: This lithofacies is interpreted as deposits of cohesive debris flows with moderate matrix content. The local matrix-supported zones indicate sufficient cohesive strength to support clasts, yet the overall lower mud content (<15%) compared to clay-rich debris flows suggests moderate viscosity and possibly shorter transport distance.

(2) Gs

Description: The Gs lithofacies is a debrite characterized by slump structures, in which neither gravel nor sand individually exceeds 50%, though their combined content is >50%. It exhibits chaotic mixing of poly-disperse clasts, sand, a clay-grade matrix, and allochthonous mudstone clasts (up to 3 m long). Clasts are poorly sorted, sub-angular, and weakly rounded. Internal plastic deformation (ductile shear) is preserved within the mudstone clasts (Fig. 5(i)).

Interpretation: This lithofacies is interpreted as a subaqueous debris-flow deposit resulting from large-scale slope failure and sediment remobilization. The internal ductile shear within mudstone clasts confirms that failure and transport occurred while the mud was still plastic (Shanmugam, 2000).

4.1.3. Sandstone lithofacies

Sandstone lithofacies are classified by grain size into heterogranular sandstone and fine–medium sandstone. Based on sedimentary structures, these are further subdivided into five subtypes: massive heterogranular sandstone (Shm), cross-stratified heterogranular sandstone (Shc), parallel-stratified heterogranular sandstone (Shp), massive fine–medium sandstone (Sfm), and parallel-stratified fine–medium sandstone (Sfp) (Fig. 6(a)–(g)).

(1) Shm

Description: Shm is a massive heterogranular sandstone. It contains well-rounded clasts (predominantly sub-rounded) and exhibits variable sorting from poor to well sorted (Fig. 6(a)).

Interpretation: This lithofacies is interpreted as deposits of rapid, unsteady sedimentation from turbulent flows under high-energy conditions. The massive structure indicates rapid deposition without sustained traction, which inhibited the development of internal stratification (Lowe, 1982).

(2) Shc

Description: The Shc lithofacies is a cross-stratified heterogranular sandstone characterized by small-scale planar cross-stratification with low dip angles (8°–20°). Clasts are moderately rounded (sub-rounded to sub-angular). Sandy grains show bedding-parallel alignment, with local floating gravels; sorting is moderate (Fig. 6(b)).

Interpretation: This lithofacies records deposition from sustained, moderate-energy traction currents. The planar cross-bedding indicates migration of dunes or ripples under stable flow. Local floating gravels point to sporadic higher-energy pulses, likely during flood events.

(3) Shp

Description: The Shp lithofacies is a heterogranular sandstone with parallel bedding. It is characterized by well-oriented sandy clasts and localized small gravels, forming units with fining-upward sequences (Fig. 6(c)). Sorting is moderate to poor, as observed in thin section (Fig. 6(d)).

Interpretation: This lithofacies is interpreted as upper-flow-regime sheet-flow deposits, reflecting waning flood conditions. Parallel bedding and clast orientation indicate high-energy plane-bed transport, while the fining-upward sequences record progressive flow deceleration during the recession phase of flood events (Zavala et al., 2006).

(4) Sfm

Description: Sfm is a massive fine–medium sandstone. It is well sorted but contains a relatively high proportion of mud (Fig. 6(e)).

Interpretation: This lithofacies is interpreted as deposits of low-energy, suspension-dominated sedimentation with minor traction reworking.

(5) Sfp

Description: The Sfp lithofacies is a parallel-stratified fine–medium sandstone. It is commonly interbedded vertically with massive sandstone, forming packages with fining-upward cycles (Fig. 6(f)). Clast sorting is moderate (Fig. 6(g)).

Interpretation: This lithofacies records periodic, moderate-energy traction currents. Each fining-upward cycle represents a single waning-flow event, in which the parallel-stratified interval marks the higher-energy phase (Zavala and Pan, 2018).

4.1.4. Siltstone lithofacies

Description: The dominant siltstone lithofacies is horizontal-laminated siltstone (Sih). It consists mainly of silt-sized grains, is typically gray to gray-green, and locally exhibits ripple lamination in silt-rich intervals (Fig. 6(h)).

Interpretation: This lithofacies represents low-energy suspension deposits in a quiet-water setting. Horizontal lamination records steady fallout of fines from a stable water mass, and the gray to gray-green color indicates deposition under reducing conditions.

4.1.5. Mudstone lithofacies

Description: The dominant mudstone lithofacies is horizontally laminated mudstone (Mh). It contains abundant clay and minor silt, has a homogeneous texture, and varies in color from gray-green to gray and dark gray (Fig. 6(i)).

Interpretation: This lithofacies represents very low-energy suspension deposits in a quiet, stable setting. Its homogeneous, clay-rich composition and horizontal lamination indicate continuous, slow settling from a stagnant water mass.

4.2. Architecture characteristics of outcrop sections

4.2.1. Types and characteristics of architectural elements

The study sections were deposited in the lacustrine steep-slope zones. The exposed mudstones are predominantly homogeneous and exhibit reduced coloration, characteristic of underwater deposition. Consequently, the preserved sedimentary record primarily represents fan-delta front deposits within the lacustrine steep-slope zones. Three types of architectural elements are recognized in conglomerate and sandstone deposits, including distributary channels, lobes, and slump deposits. Siltstone and mudstone sediments are mainly lacustrine deposits and are not within the scope of this study.

(1) Distributary channel

Description: Distributary channels are typically characterized by a flat-topped, convex-based geometry in cross-section (Fig. 7(a)). Lithologically, they are dominated by pebble to granule conglomerate and heterogranular sandstone, which display graded bedding and cross-bedding (represented by lithofacies Cpg, Cgg, Cgc, and Shc). Vertically, the deposits form fining-upward cycles with distinct basal scour surfaces, as seen in the Cpg and Cgg facies (Fig. 7(b)). The Cgc, characterized by vertically imbricated clasts, mudstone rip-up clasts, and well-developed water-escape structures, grades upward into the Shc. These channels incise into underlying dark gray mudstone and greenish siltstone (lithofacies Mh and Sih).

Interpretation: All distributary channels observed in the outcrop sections are interpreted as subaqueous distributary channels, based on their association with gray-green siltstone and gray mudstone. Cross-bedding and fining-upward cycles record sustained bedload transport and periodic flood events. These cycles, together with basal scour surfaces, reflect repeated episodes of channel erosion during flood peaks followed by deposition during waning flow (Zavala et al., 2006).

(2) Lobe

As key depositional elements, lobe deposits exhibit a flat base and a convex top in cross-section. The upper surface of the lobes is onlapped by laterally adjacent strata, indicating progressive sediment infilling along their flanks. Lithologies range from conglomerate and glutenite to sandstone, and are characterized by massive structure, graded bedding, and parallel bedding. Field observations reveal two distinct morphological types: gravel-dominated lobes, which are thicker but laterally restricted and predominantly massive; and sand-dominated lobes, which are thinner yet wider and show an increase in parallel bedding toward the lake center. Based on these pronounced differences in grain size, sedimentary structures, and geometry, we classify them as gravel lobes and sand lobes, respectively (Fig. 8; Table 1).

(A) Gravel lobe

Description: Gravel lobes are predominantly composed of conglomerate and glutenite with a wide grain-size range. They exhibit a massive structure and contain abundant mudstone rip-up clasts (represented by lithofacies Gm, Cgm, Cpm, and Ccm) (Fig. 8(a)). The median grain size within these lobes ranges from 3.26 mm to 20.58 mm (mean = 11.60 mm), and the clay content is low.

Interpretation: Gravel lobes are interpreted as progradational, tongue-shaped deposits formed by cohesive debris flows at a fan-delta front. Their massive fabric, near-vertical clasts, and abundant rip-up clasts indicate deposition by rapid flow “freezing” (Sohn et al., 1999), a process that limited lateral spreading and promoted distal elongation of the lobes (Van Dijk et al., 2009). The coarsening-upward succession from Gm to Ccm records lobe progradation and reflects an increase in flow energy during deposition (Blair and McPherson, 1998).

(B) Sand lobe

Description: Sand lobes consist predominantly of heterogranular sandstones and fine–medium sandstones, featuring graded bedding, parallel bedding and massive structure (represented by lithofacies Shm, Shp, Sfm, and Sfp). Their cross-section shows flat-based, convex-top geometries but occur as laterally extensive thin layers (Fig. 8(b)). Median grain size ranges from 0.147 mm to 1.492 mm (average 0.695 mm) with low mud content. These lobes contain parallel-stratified sandstone intercalated with oriented gravel layers (predominantly granules), forming vertically stacked coarsening-upward cycles without distinct boundaries (Fig. 8(b)).

Interpretation: Sand lobes are interpreted as distal or fringe deposits of subaqueous lobes, formed primarily by waning turbidity currents and traction currents. Unlike rapidly frozen gravel lobes, sand lobes consist of finer suspended sediments. Insufficient hydraulic resistance prevents rapid settling, facilitating lateral spreading that produces thin cross-sectional layers (Zhang et al., 2023). Deposition involves complex flow transformations between turbidity currents and traction currents.

(3) Slump body

Description: Slump deposits are developed on the left side of the Y section, proximal to the provenance area (Fig. 9(a)), with an exposed width of about 48 m, a thickness of about 3 m, and an area exceeding 140 m^2. The slump body shows abrupt lithological contacts with overlying, underlying, and adjacent rock layers within the same stratum (Fig. 9(b)). Internally, the slump deposit comprises a chaotic mixture of sandy clasts, muddy sediments, and mud gravels of varying sizes, rapidly accumulating alongside gravels of multiple grain sizes (granule, pebble, and cobble). High mud content imparts an overall gray-green to gray color to the

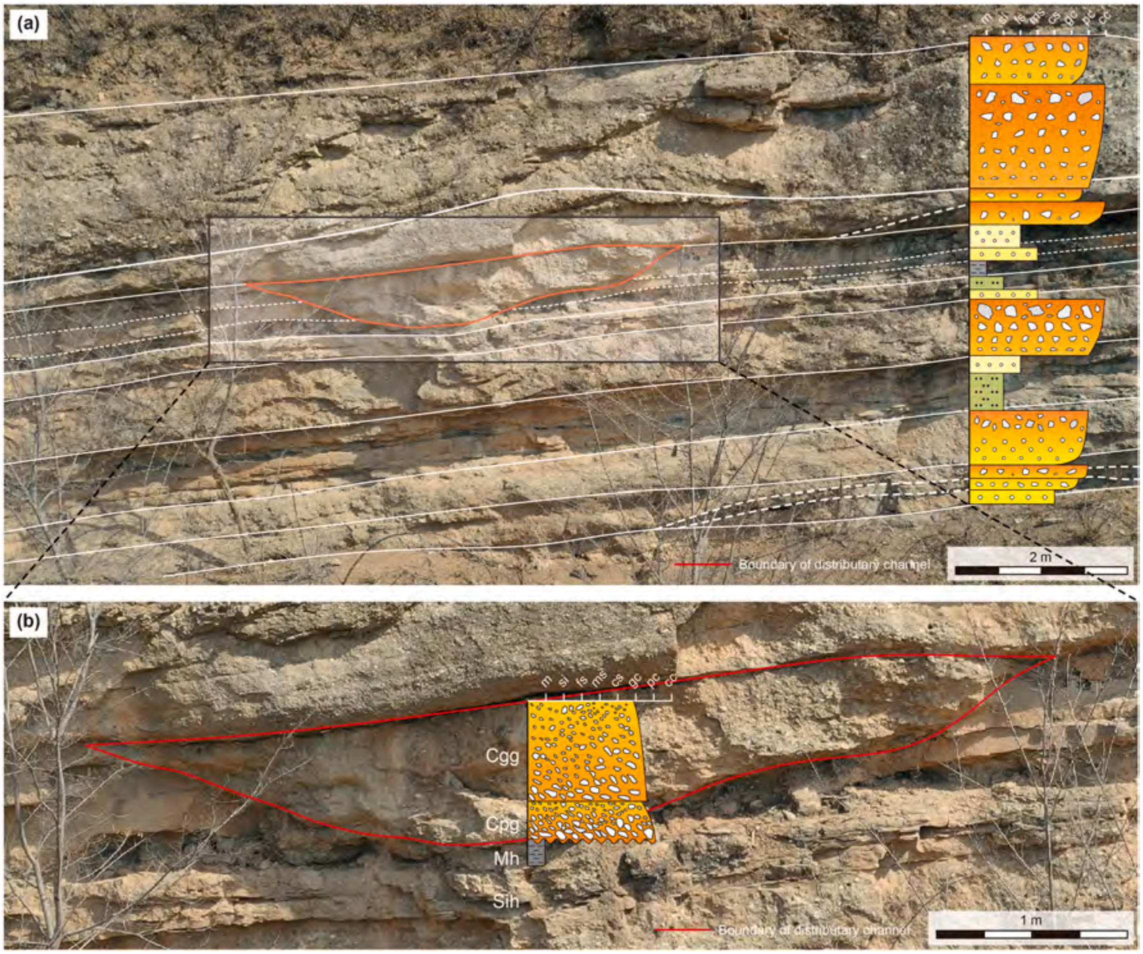

Fig. 7. Depositional architectural interfaces and lithological characteristics of distributary channel deposits. **(a)** An outcrop overview showing the architectural interfaces and lithological characteristics around representative distributary channels; **(b)** a magnified close-up showing the internal depositional characteristics of the distributary channel.

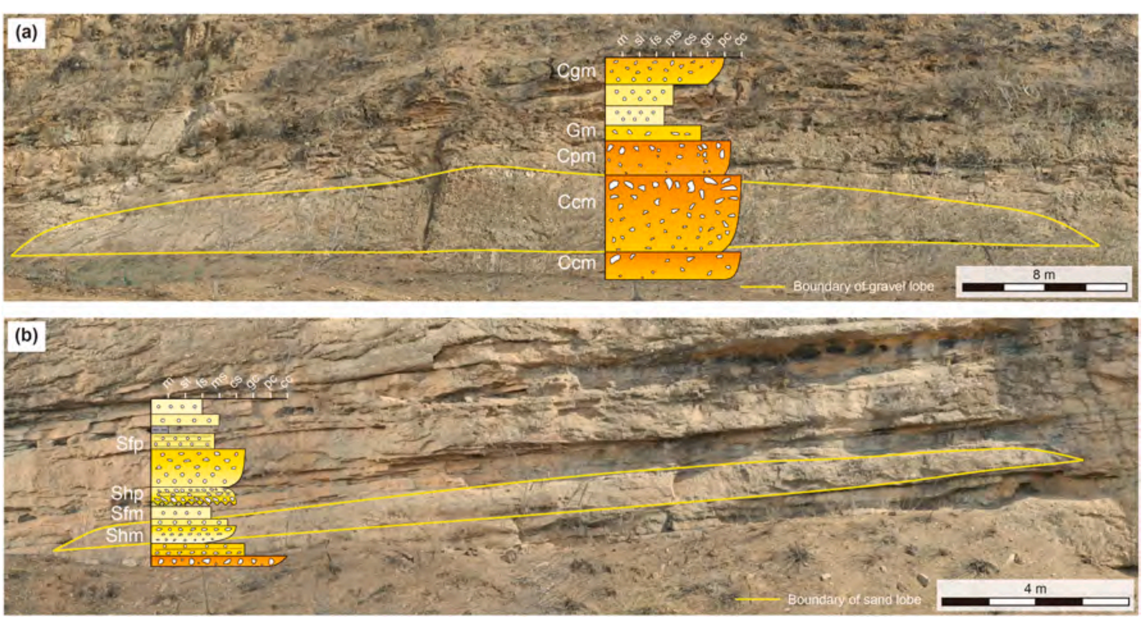

Fig. 8. Depositional architectural interfaces and lithological characteristics of lobes. **(a)** Gravel lobes are characterized by thick, coarse-grained sediments and an overall coarsening-upward grain-size trend; **(b)** sand lobes are characterized by thin beds of cross-stratified and parallel stratified sandstones, and exhibit a coarsening-upward trend.

Table 1
Diagnostic characteristics for distinguishing gravel and sand lobes.

Lobe type	D_{50}, mm	Main sedimentary structure	Width, m	Thickness, m	Width/Thickness	Stacking pattern	Interpreted flow type
Gravel lobe	3.26–20.58	Massive	16–55	1–6	4–39	Lateral migration	Debris flow
Sand lobe	0.147–1.492	Parallel bedding; graded bedding	13–58	0.2–1.8	37–146	Vertical stacking	Turbidity current; traction current

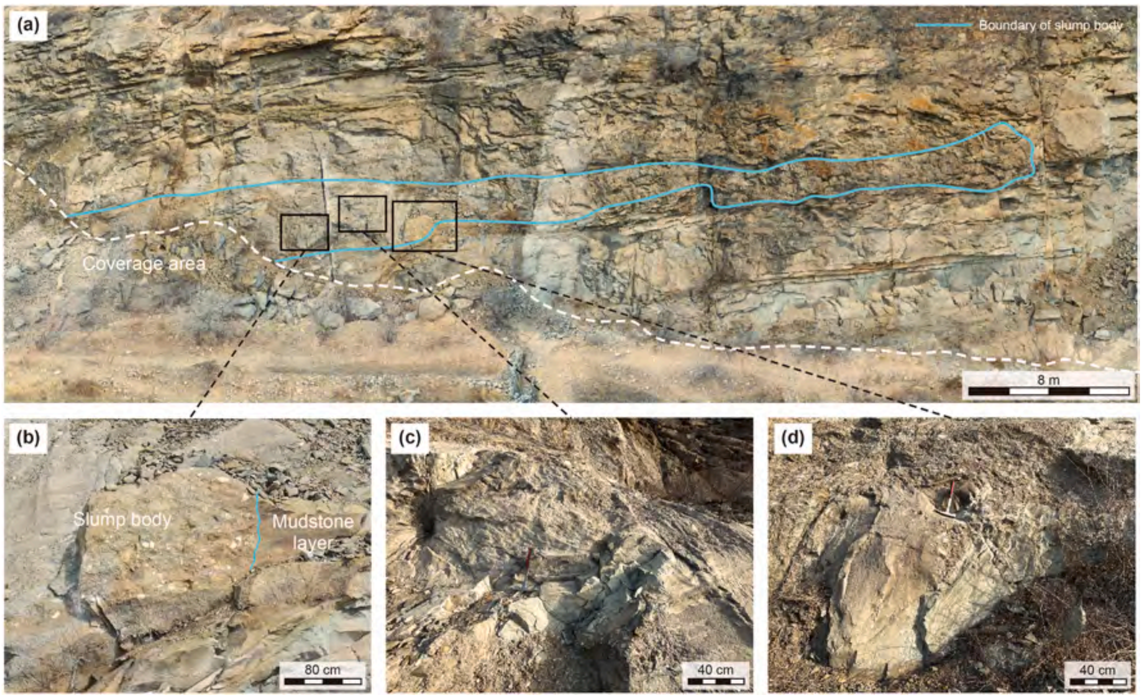

Fig. 9. Depositional architectural interfaces and internal lithological characteristics of the slump body. **(a)** An outcrop overview showing the architectural interfaces of the slump body; **(b)** abrupt contact between the glutenite and the mudstone layer; **(c)** the overturned and crumpled mudstone layer within the slump body; **(d)** a nearly vertical mudstone layer within the slump body.

deposit. Three boulder-scale mud gravels can be seen inside the slump body, which are semi-consolidated mudstone layers to be precise, the largest of which can reach 3 m. The specific manifestations are soft sediment plastic deformation such as fracture of mudstone layers, overturning and nearly upright mudstone blocks, and obvious distortion and deformation inside mudstone blocks (Fig. 9(c) and (d)).

Interpretation: It is speculated that steep slopes and high-energy flood scouring first detached semi-consolidated mudstone, forming large debris blocks that slid toward the center of the lacustrine basin (Yang et al., 2021). During the continuous sliding process, continuous scouring by high-density, sediment-laden floods combined with basal friction induced progressive twisting and deformation. The extreme slope gradient further transformed motion from sliding to collapse, resulting in layer fracturing, overturning, and block rotation.

4.2.2. Dimensions

Based on the characteristics of different types of architectural elements, particularly their lithofacies and morphological features, the spatial distribution of the fan-delta front in the study area was dissected in detail (Fig. 10). The relative development of architectural elements, including distributary channels, lobes (gravel lobes and sand lobes), slump deposits, and lacustrine mudstones, was quantified using the three-dimensional digital outcrop models derived from UAV observations of the two study sections. Results indicate that in the Y section, sand–gravel deposits constitute 83% of the section, while lacustrine mudstones represent 17%. Within the sand–gravel deposits, lobes account for 96%, with gravelly lobes and sandy lobes comprising 40% and 56%, respectively. Distributary channels and slump deposits constitute only 1% and 3%, respectively (Fig. 10(a)). In the D section, sand–gravel deposits account for 41%, and lacustrine mudstones for 59%. Among the sand–gravel deposits, lobes represent 94% (71% gravel lobes, 23% sandy lobes), while distributary channels constitute 6%. Slump deposits are absent (Fig. 10(b)).

The relationship between the width and thickness of the intact exposed single architectural elements (after projection correction for the angle between section strike and provenance direction) is shown in Fig. 11. Sand lobes exhibit the highest width-to-thickness ratios (range 37–146, average: 63), with thicknesses ranging from 0.2 m to 1.8 m and considerable lateral extents (width ranges from 13 m to 58 m). In contrast, gravel lobes show narrower width-to-thickness ratios (range 4–39; average 9.1). Distributary channels have width-to-thickness ratios of 3.6–9.8 (average 5.5) (Fig. 11(a)). The width and thickness of several types of architectural elements are strongly correlated, but there are differences. Distributary channels show a strong positive correlation (R^2= 0.92; Fig. 11(b)). Gravel lobes exhibit a negative correlation (R^2= 0.76; Fig. 11(c)), indicating greater thickness corresponds to smaller widths. Sand lobes demonstrate a positive correlation (R^2= 0.63; Fig. 11(d)). These contrasts highlight significantly different sediment grain-size controls on lobe width–thickness relationships.

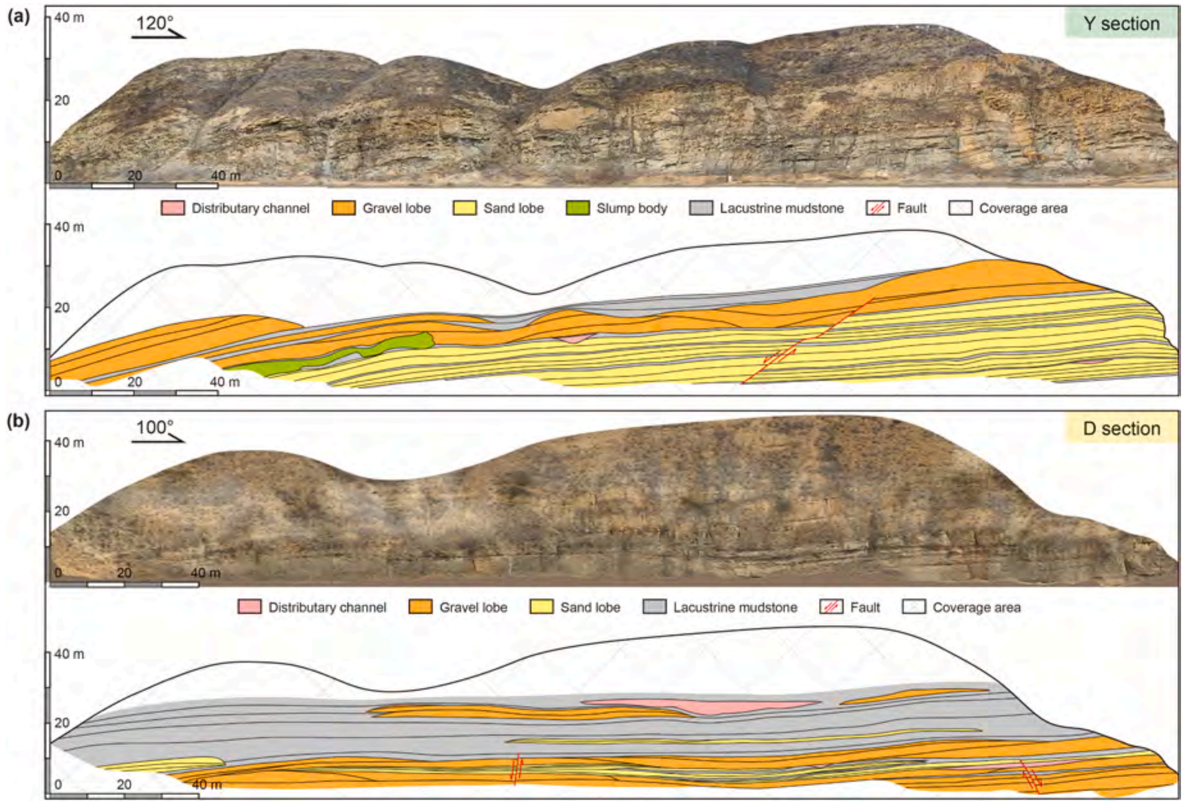

Fig. 10. 3D digital model and interpretation of architectural elements in the fan-delta front of the two study sections. **(a)** Y section; **(b)** D section.

4.2.3. Stacking patterns

The stacking patterns of sand–gravel deposits in the study sections are diverse, primarily occurring vertically and laterally. Vertical stacking styles include lobe vertical stacking, isolated lobes, distributary channels cutting into lobes, and isolated distributary channels. Lateral stacking patterns include lateral splicing of lobes and abrupt transitions from slump bodies to gravel lobes.

(1) Vertical stacking pattern. The vertical stacking relationships of lobes in the study area include multiple vertical stacking of gravel lobes and multiple vertical stacking of sandy lobes, though their stacking patterns differ significantly. Gravel lobes primarily exhibit migration-style vertical stacking, while sand lobes show thin-layered vertical stacking (Fig. 10(a)). Additionally, besides lobes interconnected through vertical stacking, isolated lobes occur in the study sections due to mudstone separation (Fig. 10(b)). Furthermore, the rare distributary channels are mostly developed above the lobes, where they shallowly cut into them. These distributary channels are typically small-scale; however, the only large-scale distributary channel is isolated and encased within lacustrine mudstone (Fig. 10(b)).

(2) Lateral stacking pattern. Lobes in the study area exhibit lateral amalgamation. Specific styles include: (i) lateral amalgamation between gravel lobes, (ii) lateral amalgamation between sand lobes, and (iii) lateral amalgamation between gravel and sand lobes. Notably, the Y section also shows lateral juxtaposition of slump bodies and lobes, more accurately representing an abrupt transition from slump bodies to gravel lobes. These slump bodies display irregular lens-shaped cross-sections with internal mixtures of sand, gravel, and mud. Their frontal zones transition abruptly into gravel lobes (Fig. 9(a) and 10(a)).

4.3. Determination and scaling of sedimentary dynamics parameters

4.3.1. Controlling factors of fan-delta development

The largest clast observed in the study area has a diameter of 0.7 m and was found within a flow layer 1.1 m thick. Substituting these values into Eq. (1) yields a calculated depositional slope of approximately 0.09 m/m (~5°) at the paleo-fan delta front. The study area is situated on the steep-slope zone of the Luanping Basin, adjacent to the Hongqi-Gangzi fault to the north (Fig. 1(b)). Although the precise slope of the source area is difficult to reconstruct, it was undoubtedly steeper than the depositional area, with significant lateral elevation changes. This steep source-to-sink gradient, combined with the rugged intermontane topography, provided the dynamic conditions necessary for fan-delta development. Furthermore, contemporaneous activity along normal faults created substantial accommodation space for its growth.

Outcrops are lobe-dominated with few distributary channels, so lobe grain size and thickness were used to calculate flow velocities. Two lobe types (gravelly and sandy) represent different architecture and were analyzed separately. Gravelly lobes average 4 m thick, with $D_{50} = 11.60$ mm and $D_{10} = 44$ mm. Eqs. (2)–(5) give an average flow velocity of 3.14 m/s (Fr = 0.502, Re = 1.3×10^7; subcritical, turbulent). Sandy lobes average 0.48 m thick, with $D_{50} = 0.695$ mm and $D_{10} = 2.380$ mm, yielding a flow velocity of 0.99 m/s (Fr = 0.449, Re = 4.7×10^5; subcritical, turbulent). Sedimentary structures are predominantly massive, with poor sorting, and low mud content. The depositional

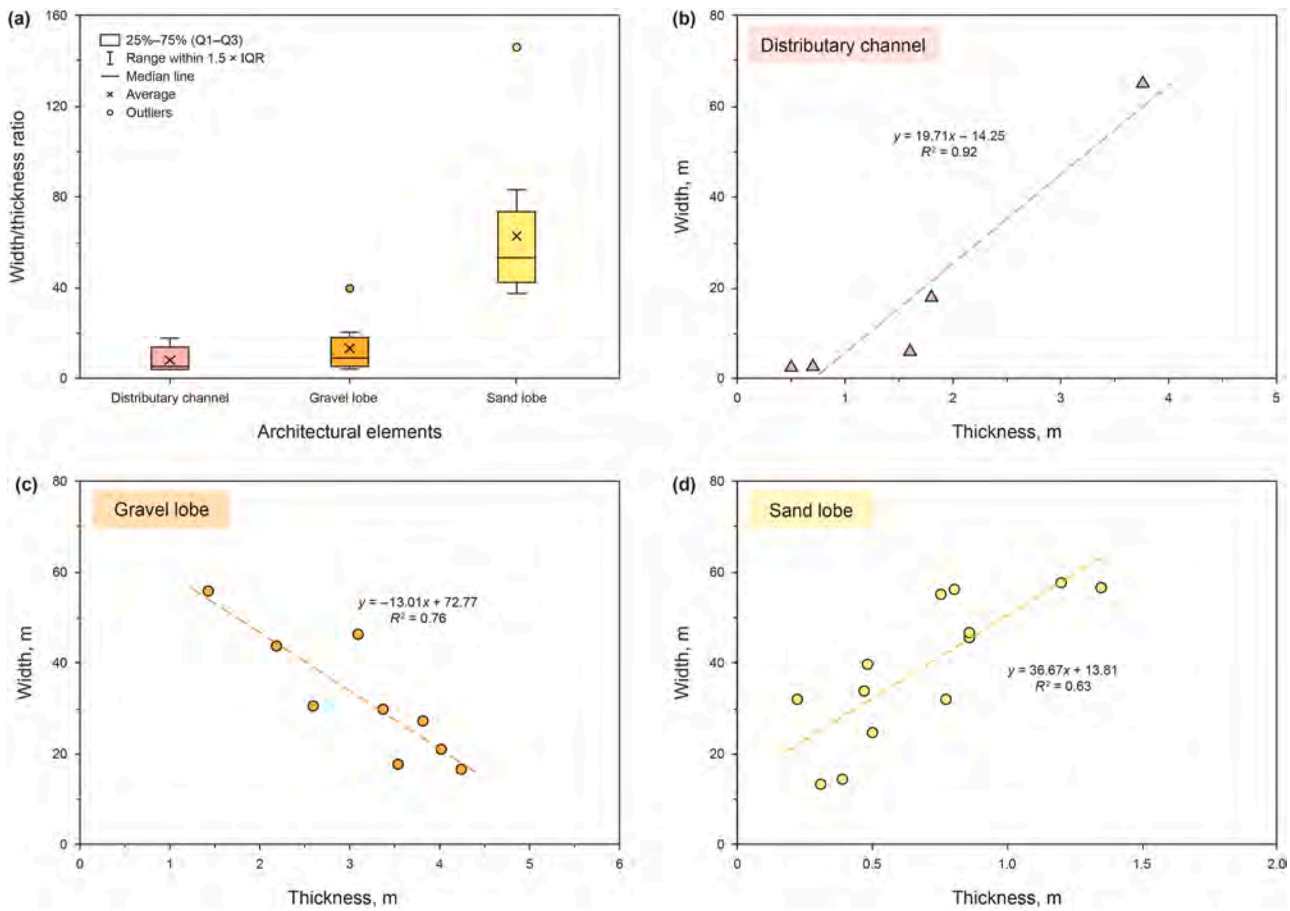

Fig. 11. Dimensions of three architectural element types measured from 3D digital models. **(a)** Box plot of width-to-thickness ratios; **(b)** scatter plot of width versus thickness for distributary channels; **(c)** scatter plot of width versus thickness for gravel lobes; **(d)** scatter plot of width versus thickness for sand lobes.

mechanisms are interpreted as sandy debris flows with minor slumps and traction currents, suggesting high sediment concentrations. The steep lateral slopes of the lacustrine basin margin promoted frequent slope failures, generating these high-density sediments. As both lobe types share the same source and depositional setting, their sediment concentrations were likely similar. The study sections reflect an arid climate with weak to moderate chemical weathering and dominant physical weathering (Sun et al., 2026). Prolonged aridity favored intermittent, large-scale, high-density floods. Thus, the coupling of arid climate and steep-slope structure controlled this fan-delta's development.

4.3.2. *Matching the experimental set-up to field observations*

The flume-tank experiments included a prototype series, designed to replicate the outcrop conditions, and an extended series with grain size as the sole variable. The prototype experiments comprised two runs, simulating the gravel-lobe and sand-lobe fan-delta types, respectively. All parameters were set according to actual depositional conditions, with hydrodynamic parameters scaled proportionally using similarity theory and standard formulas to ensure consistent sediment-transport characteristics. The most critical aspect of scaling is to ensure that key dimensionless numbers governing sediment dynamics, such as Fr, Re, τ^*, τ^*_c, and T, are matched between the experiment and the field.

(1) Depositional slope

The depositional slope in the outcrop area is approximately 0.09 m/m. A global compilation of fan-delta slopes indicates a range of 0.005–0.09 m/m. The slope of the modern Wuma fan delta in Lugu Lake, China (0.086 m/m) is very close to that of the study area. To preserve the characteristics of the source-to-sink steep-slope zones and to ensure the reliability of scaled hydrodynamic parameters, the depositional slope was not scaled. Since both types of lobes in the outcrop area correspond to source-to-sink steep-slope zones, the gradient for all three experiments was set to 0.09 m/m.

(2) Sediment concentration

Determining precise sediment concentrations from outcrops is challenging. Field investigations, however, indicate the presence of multiple transport mechanisms in the study area, including debris flows, high-density turbidity currents, and traction currents. This study employs the fluid-type classification scheme established by Shanmugam (2000) to define experimental sediment concentrations. In this framework, sandy debris flows typically have concentrations exceeding 25%, high-density turbidity currents range from 6% to 44%, and low-density turbidity currents range from 1% to 23%. As the dominant sediments in the study area are subaqueous debris flows, the corresponding terrestrial flow concentration should theoretically be greater than 25%, with even higher concentrations expected in the source area. However, experiments have shown that a volumetric concentration of 53% yields deposits consisting solely of debris flows (de Haas et al., 2016). Therefore, the theoretical concentration for our experiments needed to be set below 53%. To accurately reflect the characteristics of the steep-slope zone and to reproduce sedimentary processes such as subaqueous debris flows and turbidity currents, a series of preliminary tests were conducted at different concentrations. Based on these results, a final initial volumetric concentration of 35% was selected. This concentration ensures that surface sediments deposited in the subaqueous fan delta maintain a concentration above 25% (consistent with debris flows) while retaining the potential to be diluted and evolve into turbidity currents.

(3) Flow velocity

After obtaining hydrodynamic parameters such as the outcrop flow velocity, these parameters were scaled proportionally according to similarity theory to maintain consistency in the fluid flow regime and characteristics. Given the limitations of flow velocity in the laboratory and the relatively small difference in Fr and Re between the two lobe types, the flow velocity in this study was set to 0.32 m/s. This corresponds to Fr = 0.477, which is very close to that of the outcrop area, and Re = 1.4×10^4, indicating turbulent flow (Re > 4000) (Table 2). Therefore, the hydrodynamic conditions in the experimental and outcrop areas can be considered consistent, and the flow velocity setting is sufficient for this experimental study.

(4) Grain size

Similar to the flow velocity, grain size was proportionally converted to ensure similarity in sediment transport characteristics between the experiments and the outcrop. The primary dimensionless numbers considered in the scaling are τ^*, τ^*_c and T. Grain-size analysis shows that the D_{50} is 11.6 mm for gravel lobes and 0.695 mm for sand lobes. The average thicknesses of gravel and sand lobes in the outcrop area were 4.0 m and 0.48 m, respectively, with a sediment density of 2.7 g/cm^3. Substituting these values into Eqs. (6)–(11), the calculated τ^*, τ^*_c, and T for gravel lobes were 18.1, 0.06, and 301, respectively; while for sand lobes, the values were 36.2, 0.016, and 2237, respectively (Table 2).

To meet experimental requirements, three sediment grain sizes were prepared by mixing sand and clay of different sizes, with D_{50} values of 0.25 mm, 0.44 mm, and 0.78 mm, respectively (Fig. 12). Among these, sediment with D_{50} = 0.44 mm has τ^* = 5.6, τ^*_c = 0.017, and T = 338, which is close to the T value of gravel lobes in the outcrop area and was used as the scaled-down grain size for gravel lobes. Sediment with D_{50} = 0.25 mm has τ^* = 9.8, τ^*_c = 0.022, and T = 447. Although this T value is smaller than that of sand lobes in the outcrop area due to flume-tank size and sand grain size limitations, it is larger than that of the D_{50} = 0.44 mm sediment and exhibits stronger transport intensity (Table 2). This difference is significant at the flume-tank scale. Therefore, sediment with D_{50} = 0.25 mm was selected to represent sand lobes in this experiment. Additionally, sediment with D_{50} = 0.78 mm was prepared for extended experiments to clarify the control mechanism of grain size on architecture. Compared to the grain size used in the prototype experiment, the τ^*, τ^*_c, and T values for the 0.78 mm sediment were 3.1, 0.016, and 191, respectively, representing lower transport intensity in a coarse-grained background. In addition, it should be stated that all experimental parameters have been pre-tested to ensure the similarity between the experimental results and the field results.

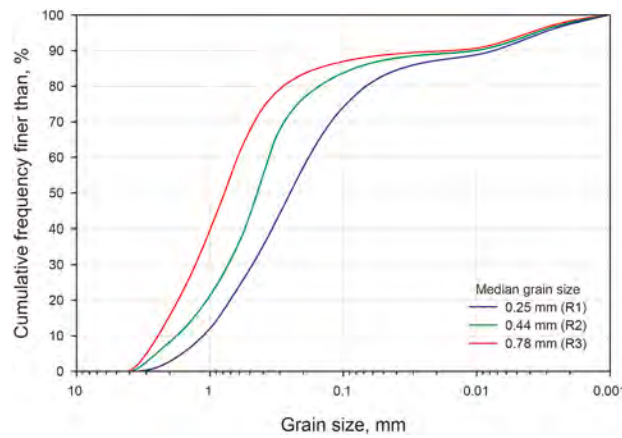

Fig. 12. Cumulative probability curves of grain size distribution of the three groups of sediments used in the flume-tank experiments.

4.4. *Architecture characteristics observed in flume-tank experiments*

4.4.1. *Morphological features*

This study conducted flume-tank simulations under lacustrine steep source-to-sink settings, testing three sediment grain-size groups as the primary variable (Table 2). The results reveal a strong grain-size control on fan-delta morphology. Both the overall depositional complex and individual lobe geometry vary significantly across experiments (Fig. 13). In the experiment R1, the fan-delta complex has a broad, fan-shaped planform (length 61.8 cm, width 94.0 cm; aspect ratio 0.66) with a smooth margin. Lobes are few and distinctly lobate, with a low planform aspect ratio (mean 1.6; range 1.3–2.0). Channels are extremely shallow (Fig. 13(a)). In the experiment R2, both the complex and individual lobes exhibit a tongue-shaped geometry (complex length 77.9 cm, width 81.5 cm; ratio 0.96). Individual lobes have a higher planform aspect ratio (mean 4.7; range 3.1–6.3). High lobe density creates pronounced margin irregularity, and channels are deeper than in R1 (Fig. 13(b)). In the experiment R3, the complex develops finger-

Table 2
Initial and boundary conditions of field and flume-tank experiments. S: slope of depositional area, m/m; C_v: volumetric sediment concentration, %; U: flow velocity, m/s; D_{50}: median grain size of sediment, mm; Fr: Froude number, dimensionless; Re: bulk Reynolds number, dimensionless; τ^*: Shields number; τ^*_c: critical Shields number; T: transportation intensity.

Field/Experiment	S, ‰	C_v, %	U, m/s	D_{50}, mm	Fr	Re	τ^*	τ^*_c	T
Sand lobe	90	/	0.99	0.695	0.449	4.7×10^5	36.2	0.016	2237
Gravel lobe	90	/	3.14	11.6	0.502	1.3×10^7	18.1	0.06	301
R1	90	35	0.32	0.25	0.477	1.4×10^4	9.8	0.022	447
R2	90	35	0.32	0.44	0.477	1.4×10^4	5.6	0.017	338
R3	90	35	0.32	0.78	0.477	1.4×10^4	3.1	0.016	191

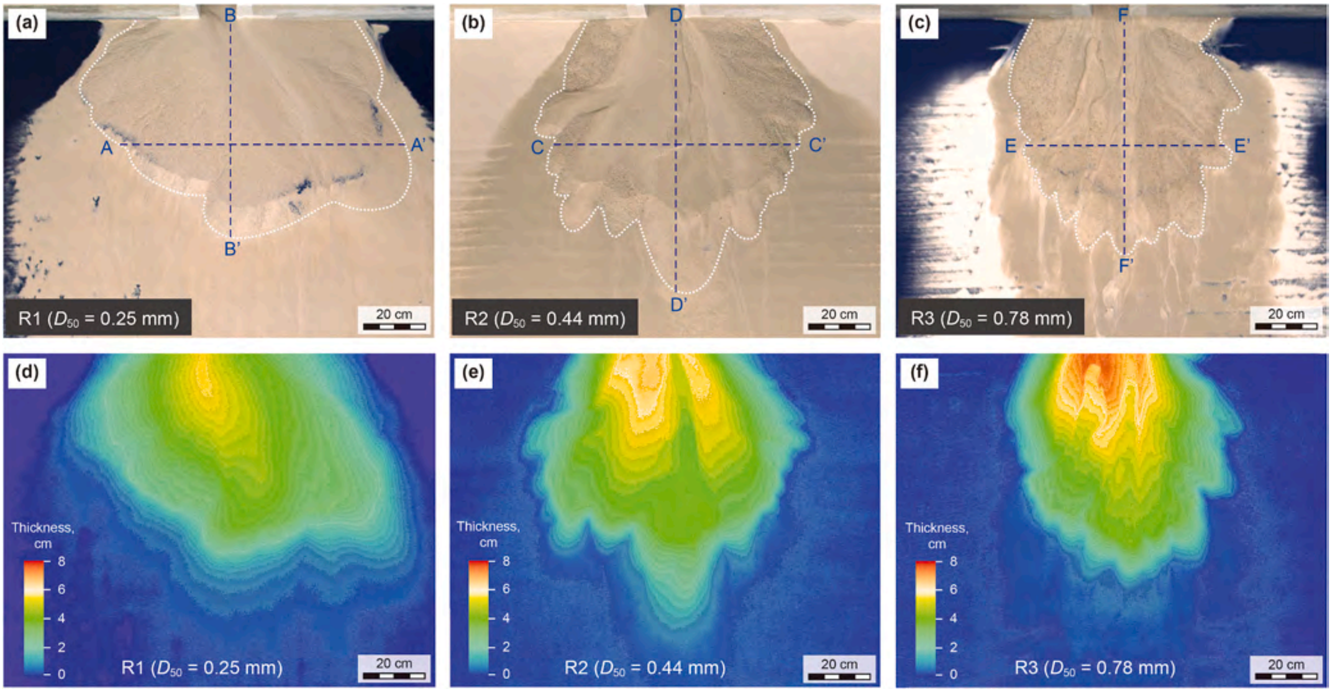

Fig. 13. Images **(a)–(c)** and thickness contour maps **(d)–(f)** of fan-delta depositional results from three experiment runs with varying grain sizes. Experiments R1 and R3 used blue sand as the substrate layer, while R2 used white sand. All substrates were 1 cm thick with identical median grain sizes.

like projections (length 76.8 cm, width 71.2 cm; ratio 1.08), dominated by numerous elongate, tongue-shaped lobes with the highest aspect ratio (mean 5.9; range 4.1–8.2). This results in the greatest margin irregularity and deepest channels, albeit with a reduced overall width (Fig. 13(c)). Integration with 3D laser-scanning-derived isopach maps further demonstrates that fine-grained systems produce deposits with greater lateral extent (divergent morphology), thinner profiles, distal spreading, and more extensive lobe termini. In contrast, coarse-grained systems form narrower (convergent morphology), thicker accumulations dominated by proximal aggradation and with reduced lobe dimensions (Fig. 13(d)–(f)).

In addition to analyzing high-definition images and 3D laser scanning models of the plain view, the experimental sections were observed, photographed, and dissected after the simulation was completed and the sediment was dried (Fig. 14). Analysis of cross- and longitudinal-sectional morphology shows that sediment grain size controls the morphology of both the fan-delta complex and its individual lobes/channels. For example, examining sections from the three experimental groups, taken perpendicular to the source direction at 40 cm from the flume-tank outlet, reveals distinct patterns. Sediments with a median grain size of 0.25 mm correspond to wider and thinner individual lobes and channels. Consequently, the resulting fan-delta complex exhibits a larger width-to-thickness ratio (width of 94.0 cm, thickness of 4.3 cm, ratio of 21.9; Fig. 14(a)). In contrast, sediments with a median grain size of 0.44 mm display a narrower and thicker cross-sectional morphology. The fan-delta complex has a slightly smaller width-to-thickness ratio (width of 81.5 cm, thickness of 4.8 cm, ratio of 17.0); individual lobes have a smaller width-to-thickness ratio, and channel incision depth increases (Fig. 14(b)). The coarsest sediments (median grain size of 0.78 mm) exhibit a consistent trend towards thicker sections, narrower widths, and enhanced channel incision capability, evident in both the fan-delta complex and individual lobes and channels. This results in the fan-delta complex having the smallest width-to-thickness ratio (width of 71.2 cm, thickness of 5.3 cm, ratio of 13.4; Fig. 14(c)).

4.4.2. Dimensions

Combined with the results of the cross-sectional architectural interpretations from the flume-tank experiments, we quantitatively assessed the relative development of the two types of architectural elements. The results show that in all experiments, lobes are the main component, while channels are extremely underdeveloped. Specifically, lobes and channels account for 98% and 2% respectively in the R1 experiment, 95% and 5% in the R2 experiment, and 96% and 4% in the R3 experiment (Fig. 14).

The relationship between the width and thickness for the two types of single architectural elements (lobes and channels) in the three flume-tank experiments is shown in Fig. 15. Among the experiments, the highest width-to-thickness ratios occurred in the R1 experiment. The sole channel had a ratio of 31.0, while lobes ranged from 16.5 to 29.1 (average 22.4). R2 exhibited lower ratios. Channels had ratios of 14.8–22.3 (average 18.6), and lobes 11.5–24.1 (average 17.5). R3 had the lowest ratios. Channels measured 6.9–14.7 (average 10.0), and lobes 2.4–15.3 (average 6.4) (Fig. 15(a)). While width and thickness were strongly correlated for single lobes across experiments, significant differences emerged by grain size. Fine-grained sediments show a strong positive correlation (R^2= 0.94; Fig. 15(b)). Medium-grained sediments exhibit a weaker correlation (R^2= 0.52; Fig. 15(c)). Coarse-grained sediments display a clear negative correlation (R^2= 0.41; Fig. 15(d)). This trend closely resembles the width–thickness relationship observed in gravel lobes from the field outcrop sections (Fig. 12(c)), demonstrating that an increase in sediment thickness corresponds to a decrease in lobe width under coarse-grained sediment conditions, while an increase in sediment thickness corresponds to an increase in the lobe width under fine-grained sediment conditions.

4.4.3. Stacking patterns

The three flume-tank experiments revealed four main stacking patterns: shallow channel downcutting of lobes, deep channel downcutting of lobes, vertical stacking of lobes, and lateral migration of lobes.

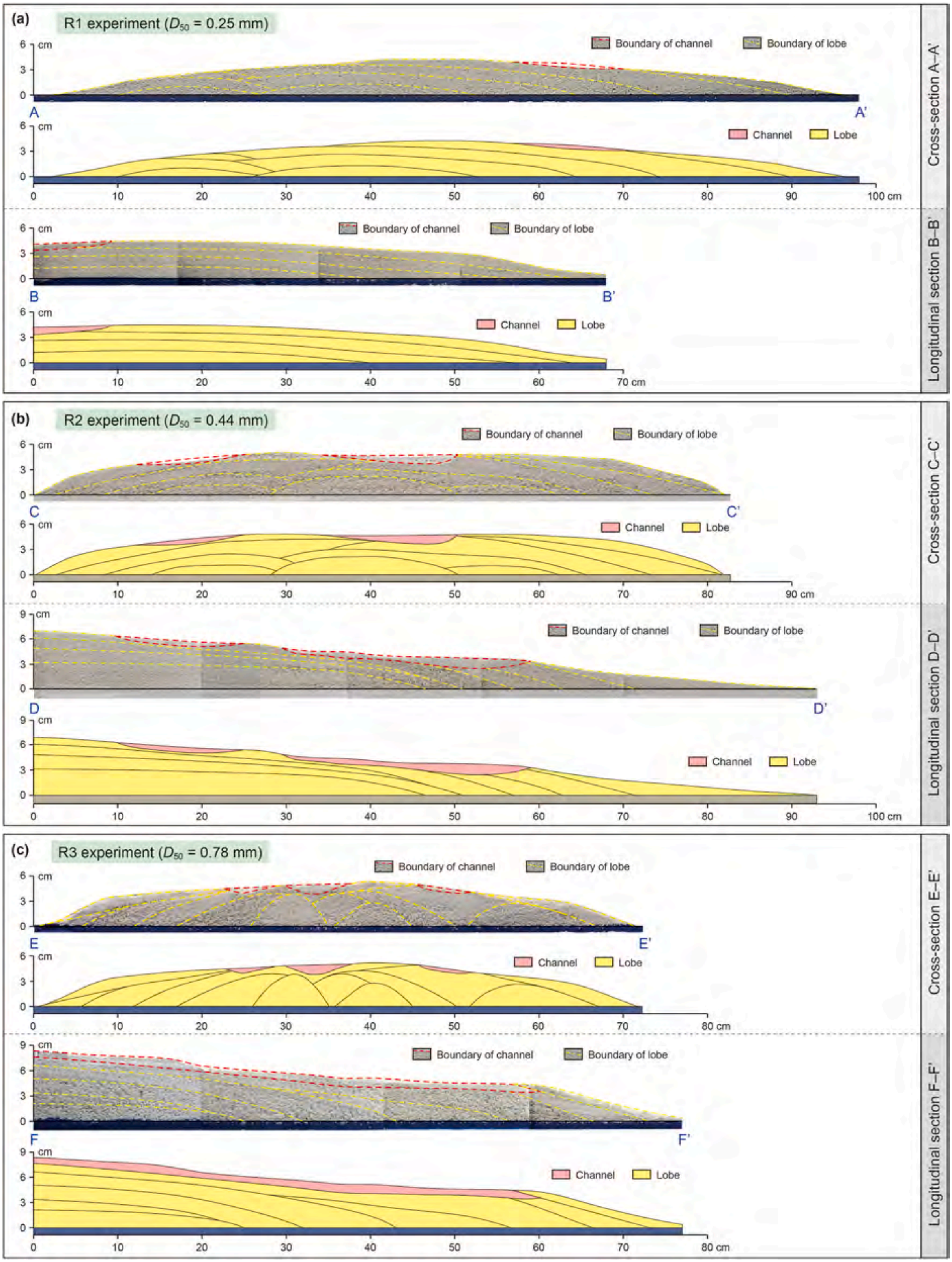

Fig. 14. Fan-delta section images and architectural interpretations from three flume-tank experiment runs with varying grain sizes. The locations of the sections are shown in Fig. 13(a)–(c).

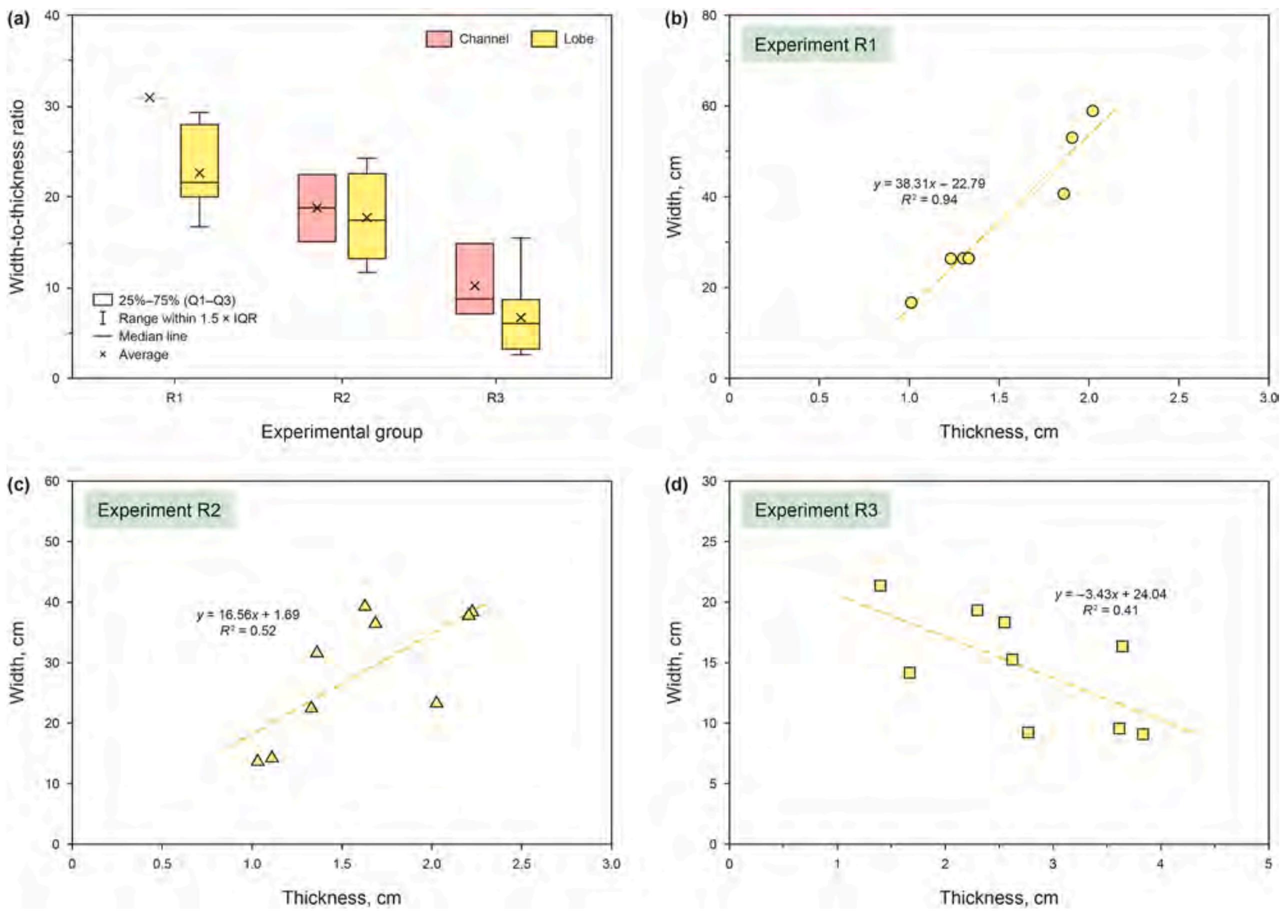

Fig. 15. Dimensions of the two architectural element types measured from 3D laser-scanning models across the three experiment runs. **(a)** Box plot of width-to-thickness ratios; **(b)** scatter plot of width versus thickness for lobes in experiment R1; **(c)** scatter plot of width versus thickness for lobes in experiment R2; **(d)** scatter plot of width versus thickness for lobes in experiment R3.

In the flume-tank simulation of fine-grained sediments, channels displayed weak downcutting erosional capacity. This primarily produced shallow channel downcutting of lobes (Fig. 14(a)). Conversely, coarser-grained sediments featured channels with strong erosional intensity, predominantly generating deep channel downcutting of lobes (Fig. 14(b) and (c)). During initial deposition stages with underdeveloped channels, different stacking patterns occurred among lobes. Sediment grain size diversity also governed the dominant stacking pattern. For example, the fine-grained R1 experiment frequently exhibited vertical stacking between lobes, while lateral migration occurred rarely and was restricted to the fan-delta margins (Fig. 13(a) and 14(a)). By contrast, the coarser-grained R2 and R3 experiments demonstrated more prevalent lateral lobe migration. Concurrently, vertical stacking frequency decreased, individual lobe numbers increased, and fan-delta complex edges developed greater irregularity (Fig. 13(b) and (c) and 14(b)–(c)).

5. Discussion

5.1. Comparison and evaluation of flume-tank experiments with field outcrops

Compared to previous works (Zhang et al., 2021, 2023), this study provides two new insights: (1) the relationship between source-to-sink slope and the development of architectural elements, and (2) the control mechanism of grain size on lobe architectural differentiation. Architectural analysis of outcrops reveals that the fan-delta system in the source-to-sink steep-slope zones are predominantly composed of lobes, with poorly developed distributary channels. These lobes are further categorized into gravel and sand lobes, each exhibiting distinct morphological characteristics, dimensions, and stacking patterns. Gravel lobes, characterized by a smaller width-to-thickness ratio, primarily undergo lateral migration of individual lobes. In contrast, sand lobes display a larger width-to-thickness ratio and typically form thin, vertically stacked layers. Moreover, the lobe morphologies produced in the experiments with varying grain sizes are highly consistent with those observed in the outcrop. Overall, grain size is negatively correlated with the width-to-thickness ratio of lobes: coarse-grained lobes tend to migrate laterally, while fine-grained lobes exhibit a vertical stacking pattern.

Compared with field observations, the flume-tank experiments more clearly reproduce certain depositional processes and plan-view distribution patterns (Wang et al., 2015). By isolating grain size as the sole variable, the experiments help identify underlying trends and reduce the randomness and interpretational ambiguity inherent in field studies. However, it is important to acknowledge the inherent simplifications of the experimental approach (de Haas et al., 2016). Due to scale and material constraints, several natural processes and architectural details are inevitably under-represented in the flume-tank experiments: (1) the full grain-size distribution and compositional heterogeneity of natural sediments; (2) the role of cohesive clay in modifying flow rheology and deposit geometry; (3) the effect of prolonged, intermittent sediment supply and associated temporal evolution of lobe complexes; and (4) secondary post-depositional modification (e.g., bioturbation and syn-depositional deformation).

Regarding the replication of depositional processes inferred from the field, the experiments successfully captured the first-order behavioural difference between high-density, poorly mobile flows (represented by the coarse-grained runs) and more fluid, distributive flows (fine-grained runs). The debris-flow processes inferred for gravel lobes were approximated by the rapid "freezing" of the coarse sediment, producing compensational stacking. The turbidity-current and tractive processes inferred for sand lobes were replicated by the sustained, distributive flows that formed sheet-like, vertically stacked deposits. Nevertheless, the flume flows represent end-member simplifications; natural events likely involved more complex transitions between debris-flow, turbulent flow and traction flow regimes, which are challenging to scale precisely in a flume tank.

Moving forward, fully leveraging physical experiments will remain a major trend in sedimentary simulation. Concurrently, ultra-high-resolution field technologies (e.g., UAV-based photogrammetry) must continue to advance. Therefore, future sedimentological research should integrate multiple lines of evidence, including field outcrops, modern sediments, subsurface well-log and seismic data, and physical/numerical simulations, to enable collaborative, multi-dimensional investigations of sedimentary systems.

5.2. Relationship between source-to-sink slope and fan-delta architectural elements

This study primarily focuses on the depositional architecture of the fan-delta front in source-to-sink steep-slope zones. Both field outcrop surveys and flume-tank experiments reveal that the main architectural elements of the fan-delta front in these steep-slope zones are lobes, with the proportion of channel elements being very low (not exceeding 6%). Considerable controversy exists regarding the architectural elements of fan-delta fronts and their degree of development. Previous studies suggest that fan-delta front elements are mainly composed of distributary-channel sand bodies, while lobes are undeveloped or small in scale (Chen et al., 2024; Jia et al., 2000; Zhang et al., 2020). Other scholars argue that distributary channels and lobes of the fan-delta front develop simultaneously, or that the fan-delta front is even composed primarily of lobes (Billi et al., 1991; Van Dijk et al., 2009; Wang et al., 2015).

As research deepens, the role of slope in controlling fan-delta systems has received increasing attention, mainly manifested in three aspects: (1) slope affects fan-delta morphology by controlling fluid flow velocity. A sufficiently steep slope maintains fluid shear stress far above the critical value, causing flow velocity to exert a greater influence on fan morphology than grain size (Harvey et al., 2005; Parker et al., 1998); (2) slope provides the primary driving force for sediment migration, governing the balance between driving force and resistance (Gao et al., 2020; Hussain et al., 2020); (3) slope influences fluid flow transformation processes and the stacking patterns of lobes in fan deltas (Sun et al., 2025). Nevertheless, the relationship between slope and architectural elements has not been systematically studied or summarized. Note that the slope discussed here refers not solely to the gradient of substrate layer but to the coupled slope of the source-to-sink system. Based on analyses of numerous Google Earth images of fan-delta source-to-sink systems, we observe that steeper depositional slopes correlate with steeper source-area gradients. Examples include: (1) the Wuma fan delta in Lugu Lake (southwestern China); (2) the Yangxi fan delta in Erhai Lake; (3) the Heimahe fan delta in the southern mountain of Qinghai Lake. Thus, this paper introduces the term "steep-slope zone" to describe source-to-sink geomorphology characterized by steep gradients in both the source area and depositional area.

Previous studies have analyzed the depositional architecture of the Sangyuan section in the gentle-slope zones of the Luanping Basin, concluding that distributary channels and lobes are the main architectural elements of the fan-delta front, accounting for 53.42% and 36.88% of the sand-gravel deposits, respectively (Zhang et al., 2023). Additionally, numerous flume experiments have focused on fan deltas in gentle-slope zones (Wang et al., 2015; Zhang et al., 2021, 2022). The prevailing view across these studies is that the channels are consistently well developed. The most representative study by Zhang et al. (2021) suggests that distributary channels and lobes are relatively well-developed in gentle-slope fan deltas. According to this work, lobes form through rapid sediment unloading after rivers enter standing water. In cross-section, distributary channels overlie lobes and deeply incise them (Fig. 16(a)). Although some experiments have simulated steep-slope fan deltas by adjusting the slope of the depositional area, the source conditions in these simulations often remain characteristic of gentle-slope catchments (Zhang et al., 2021, 2022). In contrast, the field sections and flume-tank simulations in this study involve source-to-sink steep-slope zones and their corresponding supply conditions. Both outcrops and experiments show well-developed lobes and relatively rare channels, with channels only shallowly incising lobes (Fig. 16(b)). Furthermore, recent studies of fan deltas in steep-slope zones indicate that their architecture is predominantly lobe-based, encompassing mouth bars, braided bars, sheet-flood bars, and sheet sands (Sun et al., 2025; Yang et al., 2021).

From a sequence stratigraphic perspective, the study sections and the Sangyuan section lie within the same third-order sequence and are spatially proximate. Thus, their depositional climates and parent rock conditions were similar. The key difference lies in the slope gradients across source-to-sink systems. The sections in this study are located in the steep short-axis slope zone of the Luanping Basin, adjacent to the northern provenance. Steep source-area mountains provided abundant sediment and sustained hyper-concentrated debris flows. Furthermore, steep slopes in both the source and depositional areas promoted high flow velocities. Consequently, the steep source-to-sink system exhibits high sediment concentrations and high discharge, inhibiting channel formation at mountain outlets but favoring debris-flow lobes. Upon entering standing water, these hyper-concentrated, high-discharge lobes continue advancing until fluid shear stress exceeds the combined basal friction and hydraulic resistance. Deposition occurs only when driving forces decay below a critical threshold. Conversely, gentler source-area slopes correspond to subdued mountains. Under equivalent weathering intensity, these yield less sediment, resulting in lower concentrations. The lower gradients in gentle source-to-sink systems inhibit flow acceleration. This combination of lower concentration and reduced discharge enables sediment to erode prior deposits and form channels.

5.3. Mechanisms of grain-size control on fan-delta architecture

This study conducted field section architectural dissection and flume-tank experiments on the fan deltas in the steep-slope zones of the lacustrine basin. The results indicate that different sediment grain sizes correspond to different morphologies, dimensions, and stacking patterns of the architectural elements of the fan-delta front. Previous studies have shown that the morphological

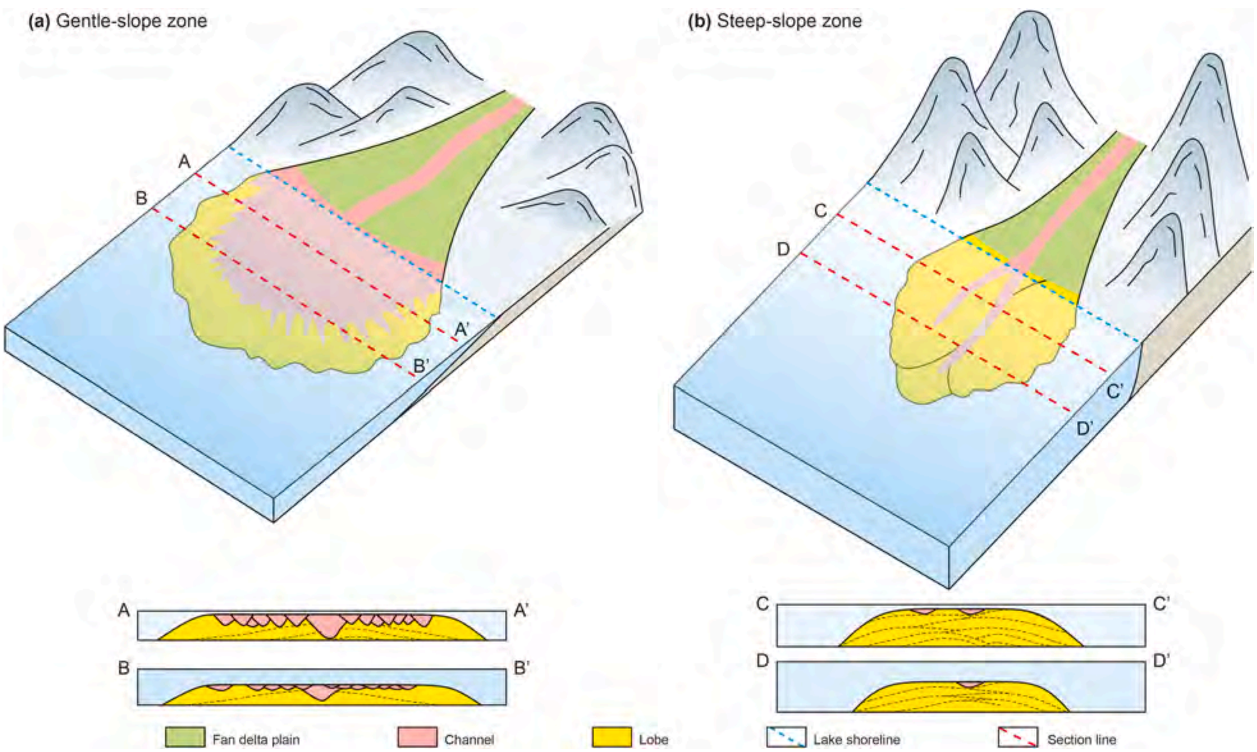

Fig. 16. Relative development patterns of architectural elements in fan delta under different slope conditions. **(a)** Gentle-slope zone; **(b)** steep-slope zone.

characteristics of the river-dominated delta is lobate or digitate due to the difference in the dominant grain size (Burpee et al., 2015; Caldwell and Edmonds, 2014; Xu et al., 2025). There are also many studies that have used physical experiments to illustrate the sedimentary evolution process and vertical grain-size rhythms of gentle-slope shallow-water fan deltas under different grain size conditions (Wang et al., 2015; Zhang et al., 2021, 2022). However, how grain size controls fan-delta architecture in lacustrine steep-slope zones remains unclear and requires analysis based on sedimentary hydrodynamic principles.

5.3.1. Mechanisms of grain-size control on the morphology and dimensions

The dimension of architectural elements is a quantitative parameter expression of morphology. From the perspective of plane morphology, a tongue-shaped plane typically exhibits a relatively long length and narrow width, while a fan-shaped plane shows a relatively short length and wide width. The width-to-thickness ratio of architectural elements also effectively characterizes cross-sectional morphological features. Previous studies demonstrate the influence of slope on lobe morphology, indicating that steeper depositional slopes increase gravitational forces on sediment. This causes lobes to advance farther, resulting in an elongated, tongue-like shape. Conversely, gentler slopes produce shorter lobes (Liu et al., 2025). Thus, the morphology of architectural elements is primarily controlled by the strength and direction of forces acting on sediments.

(1) Sediment mobility

The mobility of sediment grains is commonly quantified using the Shields number. According to Eqs. (7)–(9), the Shields number exhibits a positive correlation with the flow depth and the slope of substrate layer, and a negative correlation with the sediment density and the median grain size. Under constant conditions of flow depth, slope of substrate layer and sediment density, that is, when the average shear stress of the fluid is equal, the Shields number is negatively correlated with the sediment grain size. Consequently, coarser sediment grains correspond to a smaller Shields number, indicating reduced sediment mobility. Conversely, finer sediment grains result in greater mobility. This relationship is evident in our three experimental groups (R1, R2, R3), where $\tau^*_{R1} > \tau^*_{R2} > \tau^*_{R3}$, demonstrating a sharp decrease in mobility with increasing sediment grain size (Fig. 17).

(2) Sediment transport stability

In addition to sediment mobility, sediment transport stability is often characterized using the particle Reynolds number. According to Eq. (10), the critical Shields number depends on the particle Reynolds number. A large particle Reynolds number corresponds to a larger critical Shields number ($\tau^*_{cR1} < \tau^*_{cR2} < \tau^*_{cR3}$), indicating that a larger critical starting stress is required for coarse-grained sediments to start moving. Furthermore, previous studies demonstrate distinct flow regimes based on Re_p. When Re_p <5, the movement of particles is dominated by viscous forces. Flow around particles is hydraulically smooth, particle-fluid interaction is minimal, and sediment transport stability is high. As Re_p gradually increases, the flow transitions to a transitionally rough regime. Turbulence and vortex formation develop, reducing particle movement stability. Until Re_p >70, the flow becomes fully rough. Particle motion is highly irregular and dominated by inertial forces (de Leeuw et al., 2016; Garcia, 2008). Eq. (11) shows that for constant sediment density, the particle Reynolds number is positively correlated with grain size. In our experiments, coarser sediment corresponded to larger particle Reynolds numbers. This indicates reduced stability of sediment transport within the fluid,

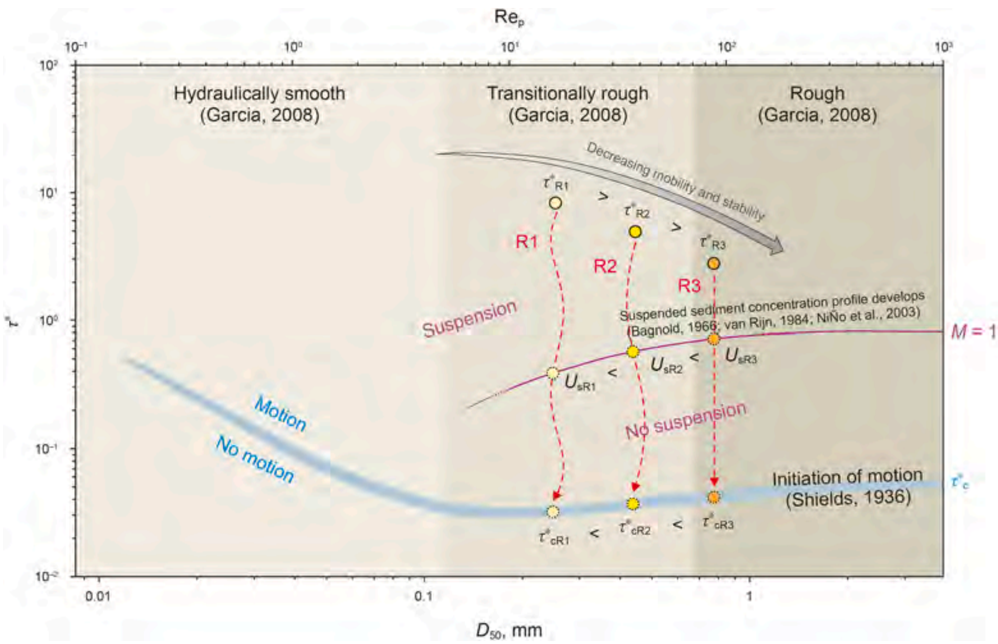

Fig. 17. Regime diagram for sediment transport showing the three experiment runs with varying grain sizes (regime boundaries based on Bagnold, 1966; de Leeuw et al., 2016; Garcia, 2008; NiÑo et al., 2003; Shields, 1936; van Rijn, 1984). *M*: settling velocity ratio.

making particles more susceptible to external disturbances and changes in motion state (Fig. 17).

(3) Settling velocity

As with the transport conditions of sediment, the settling conditions of sediment particles are equally important for the morphology and dimensions of the sediment body. The settling velocity (U_s) is used to characterize the critical velocity at which particles begin to settle after ceasing suspension, and can be calculated as follows (Bagnold, 1966; Ferguson and Church, 2004):

$$U_s = \frac{RgD_{50}^2}{C_1\mu + \sqrt{0.75C_2RgD_{50}^3}} \tag{12}$$

where R is the submerged specific gravity of the sediment in water, dimensionless; g is the gravitational acceleration, m/s^2; D_{50} is the median sediment grain size, m; $C_1 = 18$; $C_2 = 1$ (for natural sediment).

Obviously, sediments of different grain sizes exhibit distinct settling velocities. When the average flow velocity exceeds the settling velocity, the fluid has a stronger ability to transport sediments; and when the average flow velocity is equal to the settling velocity, the sediments gradually cease suspension and begin to settle. Therefore, the settling velocity ratio (M) is used to characterize the settling state of the sediment, as defined by the following equation (Parker et al., 2003):

$$M = \frac{U}{U_s} \tag{13}$$

where U is the average flow velocity, m/s; U_s is the settling velocity, m/s. When $M > 1$, sediment remains in a suspended state, and when $M = 1$, sediment exits suspension and initiates settling.

In this study, the grain size in experiment R1 was the smallest, corresponding to the smallest sediment settling velocity, while the R3 experiment corresponded to the largest settling velocity. Under the experimental conditions with the same initial average flow velocity, coarser sediments will reach their settling velocity first, cease being suspended, and settle. Conversely, finer sediments will remain suspended and transported for a longer time before settling (Fig. 17).

Under identical initial flow velocities, coarse-grained sediments reach their settling velocity more rapidly due to greater hydraulic resistance. These particles also more readily attain the critical Shields number, triggering rapid proximal deposition. Moreover, coarse sediments exhibit a lower Shields number, indicating poorer fluidity. This limited mobility inhibits lateral spreading and promotes rapid deposition near the source, forming narrow, tongue-shaped lobes with low width-to-thickness ratios. In contrast, fine-grained sediments have higher mobility (lower τ^*_c) and a lower settling velocity. These properties allow them to remain in suspension longer, be transported farther, and disperse more widely before deposition. Consequently, they form broad, lobate deposits with high width-to-thickness ratios.

Thus, in both the analyzed outcrop sections and the flume-tank experiments, coarse-grained sediments predominantly form tongue-shaped lobes with low width-to-thickness ratios, whereas fine-grained sediments produce lobate lobes with high width-to-thickness ratios (Figs. 11, 13 and 14). Furthermore, the morphology and dimensions of the fan-delta complex are governed by the geometry and scale of the individual lobes. Specifically, coarse-grained sediments yield fan-delta complexes with irregular margins and low width-to-thickness ratios, while fine-grained sediments form complexes with smoother margins and higher width-to-thickness ratios (Figs. 11, 13 and 14).

5.3.2. Mechanisms of grain-size control on stacking patterns

Previous studies have established that the deposition processes and stacking patterns of architectural elements are primarily controlled by the development of effective accommodation space (Ainsworth et al., 2018; Shen et al., 2024). Effective accommodation space is defined as the space actually filled and effectively preserved by sediments at a given depositional time-step, distinct from theoretical accommodation space generated solely by tectonic subsidence and base-level changes (Jervey, 1988; Pomar and Haq, 2016). Once effective accommodation space is filled and rapidly occupied by sediments, subsequent sediment dispersal is characterized by migration, flow diversion, and compensational stacking.

In this study, sediment grain size served as the sole experimental variable. It controls the rate at which accommodation space is filled, primarily through its influence on settling velocity. When coarse-grained sediments enter standing water, their higher settling velocity leads to rapid proximal deposition, which quickly reduces the available accommodation. Furthermore, the lower sediment mobility reflected in a low Shields number hinders the lateral diffusion of coarse grains and promotes the formation of narrow, tongue-shaped deposits. Continued sediment supply then forces newly formed lobes to migrate laterally into adjacent low-lying areas, generating a compensational stacking pattern.

In contrast, fine-grained sediments exhibit a lower settling velocity. This promotes longer transport distances and more gradual deposition, resulting in a slower accommodation-filling rate that favors vertical aggradation. Additionally, their higher mobility, which is associated with a larger Shields number, enables wider dispersal. This leads to broad, lobate morphologies with limited lateral migration, thereby creating space for vertical stacking. Consequently, both outcrop profiles and flume-tank experiments demonstrate that coarse-grained sediments exhibit multiphase compensational stacking, whereas fine-grained sediments are dominated by vertical stacking patterns.

5.4. *Architectural patterns of fan deltas in steep-slope zones with different grain sizes*

The topography, especially the slope along the source, has a significant impact on sediment flow transformation and the depositional architecture (Baas et al., 2009; Sun et al., 2025). It should be noted that the slope in this study refers not only to the bottom slope of the sedimentary basin, but also emphasizes the critical role of the slope within the intermountain supply system in the source area. Despite this, previous studies have insufficiently addressed the slope of the source system, instead emphasizing the control of the slope in the sedimentary basin on depositional architecture, and this influence primarily affects the morphological characteristics of the architectural elements (Harvey et al., 2005; Liu et al., 2025; Sun et al., 2025). However, the importance of the slope in the supply system to the depositional architecture cannot be overlooked, and the slopes of both the provenance area and the depositional area need to be systematically considered.

Previous studies have extensively investigated the sedimentary evolution, architecture, and control mechanism of shallow gentle-slope fan deltas through field outcrops and physical simulations (Zhang et al., 2021, 2022). Their architectural elements are dominated by distributary channels, where sediments rapidly unload upon entering stable water bodies to form lobes (Fig. 16(a)). Our study reveals that the fan deltas in lacustrine steep-slope zones are primarily characterized by lobes with minimal channel development. This architectural difference stems from steep-slope sediment supply conditions. Under identical weathering intensity, high-relief terrain promotes debris flow sedimentation with higher sediment concentrations. Conversely, sediment concentration and flow velocity in the gentle-slope zones are limited by source-area topography, favoring erosional channels under low-concentration conditions. Thus, the architectural elements of fan deltas in lacustrine steep-slope zones are predominantly lobes, with channels being rare and forming only as shallow gullies on lobe surfaces after flood peaks (Fig. 18).

In addition to the influence of slope on the development of architectural elements, sediment grain size is also crucial to the control of fan-delta architecture. Previous numerical simulations have indicated that sediment grain size has an impact on the morphology of fan-delta complexes, with fine-grained complexes exhibiting fan-shaped geometries and higher width-to-thickness ratios (Zhang et al., 2021). Integrating field outcrop and flume-tank experiment evidence, this study demonstrates that grain size has an impact on the morphology, dimensions, and stacking patterns of both fan-delta complexes and single architectural elements in steep-slope settings. Under identical source-basin conditions, coarse sediments have lower Shields numbers,

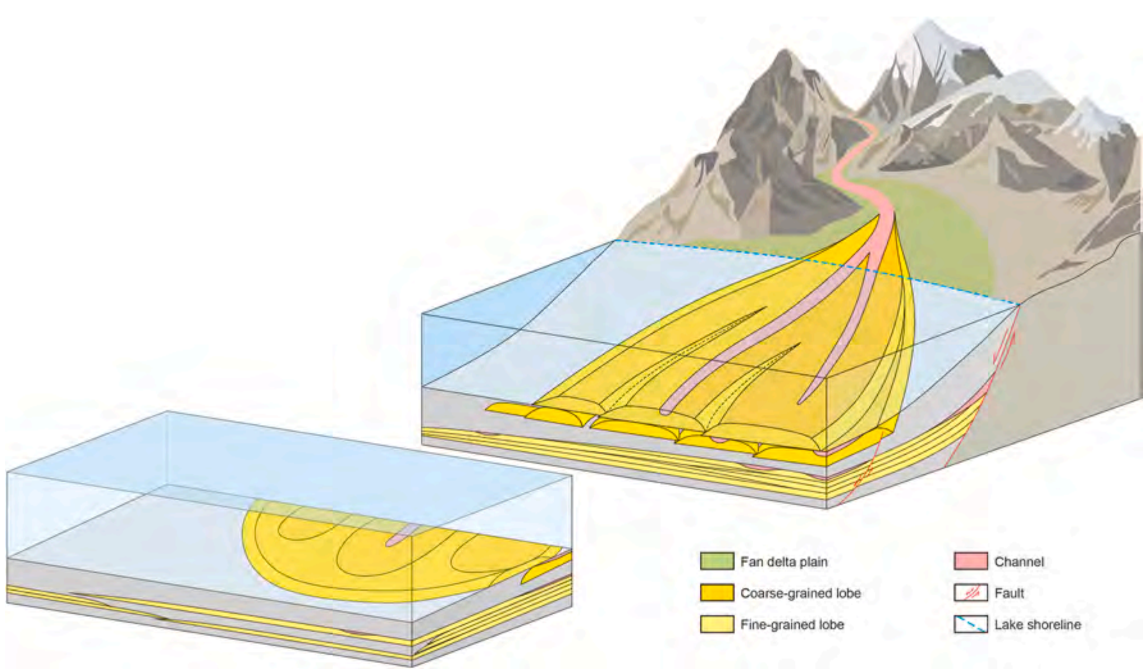

Fig. 18. Architectural patterns of fan deltas in steep-slope zones with different grain sizes. The upper part represents a coarse-grained fan delta, and the lower part represents a fine-grained fan delta.

yielding poor mobility and low stability, high sedimentation rates, and proximal accumulation. This forms tongue-shaped lobes with low width-to-thickness ratios. Rapid accumulation reduces accommodation space, causing subsequent lobes to migrate and stack preferentially in topographic lows (Fig. 18). On the contrary, fine sediments exhibit higher Shields numbers, greater mobility and high stability, and lower sedimentation rates, enabling widespread dispersal. This produces sheet-like lobes with high width-to-thickness ratios, where slow vertical settling favors thin, vertically stacked lobe successions (Fig. 18).

6. Conclusions

Our findings reveal that lacustrine fan-delta architecture is fundamentally shaped by source-to-sink slope, which sets a lobe-dominated framework, and by grain size, which dictates lobe morphology and stacking style.

(1) Lacustrine fan-deltas in source-to-sink steep-slope zones feature lobe-dominated architectures. These lobes consist of laterally extensive, high width-to-thickness ratio sand lobes and narrower, lower ratio gravel lobes. Stacking occurs via vertical aggradation and lateral migration.
(2) Under the same source-to-sink steep-slope setting, flume-tank experiments reveal that internal architecture is governed by grain size. Coarse-grained systems develop narrow, thick, finger-like lobes accompanied by deep channels and lateral migration. In contrast, fine-grained systems generate wide, thin, sheet-like lobes with shallow channels and predominantly vertical stacking.
(3) Sediment-transport regimes and architectural elements are primarily controlled by the source-area slope. Steep slopes generate high-concentration, high-velocity flows conducive to lobate spreading and inhibitory to channels. Conversely, gentle slopes promote the development of stable, erosive channels.
(4) Lacustrine fan-delta architecture in source-to-sink steep-slope zones operates through a dual control: slope dictates the overall lobe-dominated, channel-poor framework, whereas grain size modulates lobe morphology, stacking style, and channel development. This results in a continuum from coarse-grained (finger-like, laterally migrating) to fine-grained (sheet-like, vertically stacked) architectures.

CRediT authorship contribution statement

Long Sun: Writing – original draft. **Sheng-He Wu:** Writing – review & editing, Funding acquisition, Conceptualization. **Da-Li Yue:** Writing – review & editing, Funding acquisition. **Si-Chong Jiang:** Software, Methodology, Investigation. **Zhen-Hua Xu:** Visualization, Conceptualization. **Ke Zhang:** Investigation, Conceptualization. **Li-Jun Yang:** Software. **Ji-Ye Li:** Software.

Declaration of competing interest

The authors declare that they have no known competing financial interests or personal relationships that could have appeared to influence the work reported in this paper.

Acknowledgements

This research was supported by the National Natural Science Foundation of China (Grant Nos. 42272110; 42272186).

References

Ainsworth, R.B., McArthur, J.B., Lang, S.C., et al., 2018. Quantitative sequence stratigraphy. AAPG Bull. 102 (10), 1913–1939. https://doi.org/10.1306/02201817271.
Baas, J.H., Best, J.L., Peakall, J., et al., 2009. A phase diagram for turbulent, transitional, and laminar clay suspension flows. J. Sediment. Res. 79 (4), 162–183. https://doi.org/10.2110/jsr.2009.025.
Bagnold, R.A., 1966. An approach to the sediment transport problem from general physics. U. S. Geol. Surv. Prof. Pap. 422, I1–I37. https://doi.org/10.3133/pp422I.
Billi, P., Magi, M., Sagri, M., 1991. Pleistocene lacustrine fan delta deposits of the Valdarno Basin, Italy. J. Sediment. Petrol. 61 (2), 280–290. https://doi.org/10.1306/D42676EF-2B26-11D7-8648000102C1865D.
Blair, T.C., McPherson, J.G., 1998. Recent debris-flow processes and resultant form and facies of the dolomite alluvial fan, Owens Valley, California. J. Sediment. Res. 68 (5), 800–818. https://doi.org/10.2110/jsr.68.800.
Blistan, P., Kovanic, L., Zeliznaková, V., et al., 2016. Using UAV photogrammetry to document rock outcrops. Acta Montan. Slovaca 21 (2), 154–161.
Burpee, A.P., Slingerland, R.L., Edmonds, D.A., et al., 2015. Grain-size controls on the morphology and internal geometry of river-dominated deltas. J. Sediment. Res. 85 (6), 699–714. https://doi.org/10.2110/jsr.2015.39.
Caldwell, R.L., Edmonds, D.A., 2014. The effects of sediment properties on deltaic processes and morphologies: A numerical modeling study. J. Geophys. Res. Earth Surf. 119 (5), 961–982. https://doi.org/10.1002/2013JF002965.
Chen, B.T., Ma, L., Hong, L., et al., 2024. Sedimentary evolution and controlling factors of fan Delta and slump fan complex deposition in a steep slope Belt of a faulted basin: A case study from the Cretaceous deposits of the A sag in Melut Basin, Central Africa. Acta Sedimentol. Sin. 42 (3), 1058–1072. https://doi.org/10.14027/j.issn.1000-0550.2022.087 (in Chinese).
Cope, T., Luo, P., Zhang, X.Y., et al., 2010. Structural controls on facies distribution in a small half-graben basin: Luanping Basin, Northeast China. Basin Res. 22 (1), 33–44. https://doi.org/10.1111/j.1365-2117.2009.00417.x.
Cope, T.D., Graham, S.A., 2007. Upper crustal response to Mesozoic tectonism in Western Liaoning, North China, and implications for lithospheric delamination. Geol. Soc. Lond. Spec. Publ. 280 (1), 201–222. https://doi.org/10.1144/SP280.10.
de Haas, T., van den Berg, W., Braat, L., et al., 2016. Autogenic avulsion, channelization and backfilling dynamics of debris-flow fans. Sedimentology 63 (6), 1596–1619. https://doi.org/10.1111/sed.12275.
de Leeuw, J., Eggenhuisen, J.T., Cartigny, M.J.B., 2016. Morphodynamics of submarine channel inception revealed by new experimental approach. Nat. Commun. 7, 10886. https://doi.org/10.1038/ncomms10886.
Fang, Y., Olsen, P., Zheng, D., et al., 2022. A new astronomical time scale for the early Jehol Biota in the Luanping Basin, northeastern China. Palaeogeogr. Palaeoclimatol. Palaeoecol. 607, 111273. https://doi.org/10.1016/j.palaeo.2022.111273.
Ferguson, R.I., Church, M., 2004. A simple universal equation for grain settling velocity. J. Sediment. Res. 74 (6), 933–937. https://doi.org/10.1306/051204740933.
Gao, C.L., Ji, Y.L., Wu, C.L., et al., 2020. Facies and depositional model of alluvial fan dominated by episodic flood events in arid conditions: An example from the Quaternary Poplar Fan, north-western China. Sedimentology 67 (4), 1750–1796. https://doi.org/10.1111/sed.12684.
Garcia, M., 2008. Sedimentation Engineering: Processes, Measurements, Modeling, and Practice. American Society of Civil Engineers, Reston. https://doi.org/10.1061/9780784408148.
Geleynse, N., Storms, J.E.A., Walstra, D.J.R., et al., 2011. Controls on river delta formation; insights from numerical modelling. Earth Planet Sci. Lett. 302 (1–2), 217–226. https://doi.org/10.1016/j.epsl.2010.12.013.
Harvey, A.M., Mather, A.E., Stokes, M., 2005. Alluvial fans: Geomorphology, sedimentology, dynamics — Introduction. A review of alluvial-fan research. Geol. Soc. Lond. Spec. Publ. 251, 1–7. https://doi.org/10.1144/gsl.sp.2005.251.01.01.
Holmes, A., 1945. Principles of physical geology. GFF (Geol. Foren. Stockh. Forh.) 67 (1), 115–116. https://doi.org/10.1080/11035894509446436.
Hussain, A., Haughton, P.D.W., Shannon, P.M., et al., 2020. High-resolution X-ray fluorescence profiling of hybrid event beds: Implications for sediment gravity flow behaviour and deposit structure. Sedimentology 67 (6), 2850–2882. https://doi.org/10.1111/sed.12722.
Jervey, M.T., 1988. Quantitative geological modeling of siliciclastic rock sequences and their seismic expression. In: Wilgus, C.K., Hastings, B.S., Posamentier, H., et al. (Eds.), Sea-Level Changes: An Intergrated Approach, vol. 42. SEPM Special Publicaiton, pp. 47–69. https://doi.org/10.2110/pec.88.01.0047.
Jia, A.L., Mu, L.X., Chen, L., et al., 2000. Approach for detailed study of reservoir outcrop. Acta Pet. Sin. 21 (4), 105–108. https://doi.org/10.7623/syxb200004020 (in Chinese).
Jia, H.B., Ji, H.C., Yu, J.F., et al., 2020. Sediment supply control on the delivery of sediments to deep-lacustrine environment: A case study from Luanping Basin, northern China. Geol. J. 55 (5), 3679–3693. https://doi.org/10.1002/gj.3608.
Kataoka, K., Nakajo, T., 2004. Flow transformation and depositional organization of debris flow-hyperconcentrated flow-streamflow spectrum in volcanic fan-delta setting: The Pleistocene Lower and Middle Formations, Yachiho Group, central Japan. Jour. Sed. Soc. Japan 59 (59), 17–26. https://doi.org/10.4096/jssj1995.59.17.

Kim, S.B., Blair, T.C., McPherson, J.G., 1995. Alluvial fans and their natural distinction from rivers based on morphology, hydraulic processes, sedimentary processes, and facies assemblages; discussion and reply. J. Sediment. Res. 65 (4a), 706–711. https://doi.org/10.1306/d42681b2-2b26-11d7-8648000102c1865d.
Li, J., Liu, Z., Liu, J.P., et al., 2021. Transformation of sediment delivery and dispersal patterns controlled by relay-ramp evolution along the boundary fault of a lacustrine rift: The Eocene Shahejie Formation, Dongying Sag, Bohai Bay Basin, NE China. Mar. Petrol. Geol. 128, 105044. https://doi.org/10.1016/j.marpetgeo.2021.105044.
Liu, B.B., Tan, C.P., Yu, X.H., et al., 2019. Sedimentary characteristics and controls of a retreating, coarse-grained fan-delta system in the Lower Triassic, Mahu Depression, northwestern China. Geol. J. 54 (3), 1141–1159. https://doi.org/10.1002/gj.3215.
Liu, M.C., Wu, S.H., Yue, D.L., et al., 2025. Palaeogeomorphological control on the depositional architecture of lacustrine gravity-flow deposits in a depression lacustrine basin: A case study of the Triassic Yanchang Formation, southern Ordos Basin, China. J. Palaeogeogr. 14 (2), 476–500. https://doi.org/10.1016/j.jop.2025.01.003.
Lowe, D.R., 1982. Sediment gravity flows; II, depositional models with special reference to the deposits of high-density turbidity currents. J. Sediment. Res. 52 (1), 279–297. https://doi.org/10.1306/212f7f31-2b24-11d7-8648000102c1865d.
Ma, Y., Yang, H., Ma, Y., et al., 2023. Geochemical characteristics of shales from Upper Carboniferous Yanghugou Formation in Weiningbeishan area, China: Implication for provenance, source weathering and tectonic setting. Mar. Petrol. Geol. 149, 106082. https://doi.org/10.1016/j.marpetgeo.2022.106082.
McPherson, J.G., Shanmugam, G., Moiola, R.J., 1987. Fan-deltas and braid deltas: Varieties of coarse-grained deltas. Geol. Soc. Am. Bull. 99 (3), 331–340. https://doi.org/10.1130/0016-7606(1987)99<331:FABDVO>2.0.CO;2.
Milana, J.P., Tietze, K.W., 2002. Three-dimensional analogue modelling of an alluvial basin margin affected by hydrological cycles: Processes and resulting depositional sequences. Basin Res. 14 (3), 237–264. https://doi.org/10.1046/j.1365-2117.2002.00188.x.
NiÑo, Y., Lopez, F., Garcia, M., 2003. Threshold for particle entrainment into suspension. Sedimentology 50, 247–263. https://doi.org/10.1046/j.1365-3091.2003.00551.x.
Nota, P.J., Zhang, X., Liu, H., et al., 2024. Effects of upstream and downstream boundary conditions on lacustrine shallow-water delta morphologies: A numerical modeling approach. Mar. Petrol. Geol. 167, 106966. https://doi.org/10.1016/j.marpetgeo.2024.106966.
Pan, S., Jiang, Z., Zhang, Y., et al., 2021. Geochemical characteristics of the Lower Cretaceous Xiguayuan Formation mudrocks in the Luanping Basin, northern China: Implications for the hydrocarbon generation potential and sedimentary environments. Mar. Petrol. Geol. 133, 105256. https://doi.org/10.1016/j.marpetgeo.2021.105256.
Parker, G., Paola, C., Whipple, K.X., et al., 1998. Alluvial fans formed by channelized fluvial and sheet flow. I: Theory. J. Hydraul. Eng. 124 (10), 985–995. https://doi.org/10.1061/(ASCE)0733-9429(1998)124:10(985).
Parker, G., Toro-Escobar, C.M., Ramey, M., et al., 2003. Effect of floodwater extraction on mountain stream morphology. J. Hydraul. Eng. 129 (11), 885–895. https://doi.org/10.1061/(ASCE)0733-9429(2003)129:11(885).
Pomar, L., Haq, B.U., 2016. Decoding depositional sequences in carbonate systems: Concepts vs experience. Global Planet. Change 146, 190–225. https://doi.org/10.1016/j.gloplacha.2016.10.001.
Postma, G., 1990. Depositional architecture and facies of river and fan deltas: A synthesis. In: Colella, A., Prior, D.B. (Eds.), Coarse-Grained Deltas. Wiley, pp. 13–27. https://doi.org/10.1002/9781444303858.ch2.
Shanmugam, G., 2000. 50 years of the turbidite paradigm (1950s—1990s): Deep-water processes and facies models—A critical perspective. Mar. Petrol. Geol. 17 (2), 285–342. https://doi.org/10.1016/S0264-8172(99)00011-2.
Shen, L.Y., Pan, R.F., Lv, H.T., et al., 2024. Quantitative analysis of total accommodation space based on sedimentary simulation. Earth Sci. Front. 31 (2), 391–401. https://doi.org/10.13745/j.esf.sf.2023.9.1 (in Chinese).
Shields, A., 1936. Anwendung der Ahnlichkeitsmechanik und der Turbulenzforschung auf die Geschiebebewegung. Technical University Berlin, Berlin. Doctoral Thesis.
Sidorchuk, A.Y., Borisova, O.K., 2000. Method of paleogeographical analogues in paleohydrological reconstructions. Quat. Int. 72 (1), 95–106. https://doi.org/10.1016/S1040-6182(00)00025-2.
Sohn, Y.K., Rhee, C.W., Kim, B.C., 1999. Debris flow and hyperconcentrated flood-flow deposits in an alluvial fan, northwestern part of the Cretaceous Yongdong Basin, Central Korea. J. Geol. 107 (1), 111–132. https://doi.org/10.1086/314334.
Sun, H.W., Li, S.L., Li, P., et al., 2025. Morpho-dynamics in fan deltas: Effect of topography on flow transformation, facies distribution and graded profile evolution, a case study in XLG fan delta. Pet. Sci. 22 (3), 1021–1040. https://doi.org/10.1016/j.petsci.2024.12.028.
Sun, L., Wu, S.H., Yue, D.L., et al., 2024. Mineralogical and geochemical characteristics of mudstones from the Lower Cretaceous Prosopis Formation in the Bongor Basin, Chad: Implications for provenance, paleoenvironment and organic matter enrichment. Mar. Petrol. Geol. 168, 107031. https://doi.org/10.1016/j.marpetgeo.2024.107031.
Sun, L., Wu, S.H., Yue, D.L., et al., 2026. Palaeoweathering and palaeoclimate of the Lower Cretaceous Upper Xiguayuan Formation in the Luanping Basin, North China: Implications for early Aptian global cooling. J. Palaeogeogr. 15 (1), 100295. https://doi.org/10.1016/j.jop.2025.100295.
Tan, M., Zhu, X., Geng, M., et al., 2017. The occurrence and transformation of lacustrine sediment gravity flow related to depositional variation and paleoclimate in the Lower Cretaceous Prosopis Formation of the Bongor Basin, Chad. J. Afr. Earth Sci. 134, 134–148. https://doi.org/10.1016/j.jafrearsci.2017.06.003.
Tanaka, J., Maejima, W., 1995. Fan-delta sedimentation on the basin margin slope of the Cretaceous, strike-slip Izumi Basin, Southwestern Japan. Sediment. Geol. 98 (1–4), 205–213. https://doi.org/10.1016/0037-0738(95)00033-5.
Van Dijk, M., Kleinhans, M.G., Postma, G., et al., 2012. Contrasting morphodynamics in alluvial fans and fan deltas: Effect of the downstream boundary. Sedimentology 59 (7), 2125–2145. https://doi.org/10.1111/j.1365-3091.2012.01337.x.
Van Dijk, M., Postma, G., Kleinhans, M.G., 2009. Autocyclic behaviour of fan deltas: An analogue experimental study. Sedimentology 56 (5), 1569–1589. https://doi.org/10.1111/j.1365-3091.2008.01047.x.
van Rijn, L.C., 1984. Sediment transport, part II: Suspended load transport. J. Hydraul. Eng. 110 (11), 1613–1641. https://doi.org/10.1061/(ASCE)0733-9429(1984)110:11(1613.
Wang, J.H., Jiang, Z.X., Zhang, Y.F., et al., 2015. Flume tank study of surface morphology and stratigraphy of a fan delta. Terra Nova 27 (1), 42–53. https://doi.org/10.1111/ter.12131.
Wei, H.H., Meng, Q.R., Wu, G.L., et al., 2012. Multiple controls on rift basin sedimentation in volcanic settings: Insights from the anatomy of a small Early Cretaceous basin in the Yanshan Belt, northern North China. Geol. Soc. Am. Bull. 124, 380–399. https://doi.org/10.1130/B30495.1.
Whipple, K.X., Parker, G., Paola, C., et al., 1998. Channel dynamics, sediment transport, and the slope of alluvial fans: Experimental study. J. Geol. 106 (6), 677–694. https://doi.org/10.1086/516053.
Wu, F.D., Chen, Y.J., Li, Y., et al., 2000. Tectonic evolutions and their control on development of fan deltaic depositional system in the Luanping Basin. Geoscience 14 (2), 179–184 (in Chinese).
Wu, S.H., Xiong, Q.H., Gong, Y.J., et al., 1994. Steep and gentle slope-pattern fan deltas and their potential as hydrocarbon reservoir. Acta Pet. Sin. 15 (S1), 52–59. https://doi.org/10.7623/syxb1994S1007 (in Chinese).
Wu, W.T., Tang, Y., Zhao, J.Z., et al., 2025. Model of tight conglomerate oil accumulation in the Mahu Sag, Junggar Basin, Northwest China. J. Earth Sci. 36 (3), 1149–1167. https://doi.org/10.1007/s12583-023-1840-4.
Xu, Z.H., Wu, S.H., Plink-Björklund, P., et al., 2025. Autocyclic switching processes and architecture of lobes in river-dominated lacustrine deltas. J. Palaeogeogr. 14 (1), 126–140. https://doi.org/10.1016/j.jop.2024.12.004.
Yan, D., Xu, H., Xu, Z., et al., 2020. Sedimentary architecture of hyperpycnal flow deposits: Cretaceous Sangyuan outcrop, from the Luanping Basin, North East China. Mar. Petrol. Geol. 121, 104593. https://doi.org/10.1016/j.marpetgeo.2020.104593.
Yang, B.L., Qiu, L.W., Yang, Y.Q., et al., 2021. Sedimentary characteristics and transport mechanism of subaqueous coarse clastic rocks in the Lower Cretaceous Xiguayuan Formation in the steep slope zone of Luanping Basin. Earth Sci. 46 (9), 3258–3277 (in Chinese).
Yin, S.L., Zhu, B.Y., Guo, H.P., et al., 2023. Architectural model of a dryland gravel braided river, based on 3D UAV oblique photogrammetric data: A case study of west Dalongkou River in eastern Xinjiang, China. Acta Geol. Sin. Engl. Ed. 97 (1), 269–285. https://doi.org/10.1111/1755-6724.14967.
Yu, X.H., Qu, J.H., Tan, C.P., et al., 2014. Conglomerate lithofacies and origin models of fan deltas of Baikouquan Formation in Mahu Sag, Junggar Basin. Xinjing Pet. Geol. 35 (6), 619–627 (in Chinese).
Yuan, X.D., Zhang, Y.F., Jiang, Z.X., et al., 2025. Formation mechanism and geological significance of shale reservoirs in Cretaceous continental faulted basins of the Yanshan Tectonic Belt, northeastern China: A case study of the Luanping Basin. J. Asian Earth Sci. 280, 106472. https://doi.org/10.1016/j.jseaes.2024.106472.
Zavala, C., Pan, S.X., 2018. Hyperpycnal flows and hyperpycnites: Origin and distinctive characteristics. Lit. Res. 30 (1), 1–27. https://doi.org/10.3969/j.issn.1673-8926.2018.01.001 (in Chinese).
Zavala, C., Ponce, J.J., Arcuri, M., et al., 2006. Ancient lacustrine hyperpycnites: A depositional model from a case study in the Rayoso Formation (Cretaceous) of west-central Argentina. J. Sediment. Res. 76 (1), 41–59. https://doi.org/10.2110/jsr.2006.12.
Zhang, C.M., Zhu, R., Guo, X.G., et al., 2020. Arid fluvial fan delta–fluvial fan transition: Implications of Huangyangquan fan area. Earth Sci. 45 (5), 1791–1806 (in Chinese).
Zhang, K., Wu, S.H., Feng, W.J., et al., 2021. Experimental study of fan delta evolution: Autogenic cycles of fully confined channelized flow and small secondary channelized flows. Sediment. Geol. 426, 106024. https://doi.org/10.1016/j.sedgeo.2021.106024.
Zhang, K., Wu, S.H., Wang, H.H., et al., 2023. Sedimentary architecture of shallow-water fan-delta front in a lacustrine basin: Sangyuan section of Lower Cretaceous Xiguayuan Formation, Luanping Basin, Northeast China. Swiss J. Geosci. 116, 3. https://doi.org/10.1186/s00015-023-00432-5.
Zhang, K., Wu, S.H., Wang, J.J., et al., 2022. Vertical grain-size trend of mouth bar in lacustrine fan delta: Flume experiments. Pet. Sci. 19 (5), 1964–1977. https://doi.org/10.1016/j.petsci.2022.03.024.